

Analysis of and solution to the polar numerical noise within the shallow-water model on the latitude-longitude grid

Jianghao Li^{1,3}, Bin Wang^{1,2,3}, Li Dong^{1,3}

¹State Key Laboratory of Numerical Modeling for Atmospheric Sciences and Geophysical Fluid Dynamics,

Institute of Atmospheric Physics, Chinese Academy of Sciences, Beijing, China

²Ministry of Education Key Laboratory for Earth System Modeling, Department of Earth System

Science, Tsinghua University, Beijing, China

³University of Chinese Academy of Sciences, Beijing, China

Key Points:

- The vector-invariant form of the horizontal momentum equations is preferred due to the explicit calculation of potential vorticity.
- The polar noise on the latlon grid with zonal wind component staggered on the pole is eliminated by redefining the polar vorticity.

Abstract

This study conducts an analysis of the polar numerical noise in the barotropic shallow-water version of the Grid-point Atmospheric Model of IAP LASG (GAMIL-SW) and provides a good solution to the problem. GAMIL-SW suffers from numerical noise in the polar region in some ideal test cases, which is likely to be detrimental to the full physical model. The noise is suspected to be related to the nonlinear advection term in the momentum equation. Thus, a new shallow-water model with a vector-invariant form of the momentum equation is developed on the latitude-longitude grid to analyze the polar noise. It is found that the version with meridional wind component staggered on the pole is free from noise, while the version with zonal wind component staggered on the pole is still contaminated. By redefining the polar relative vorticity, the polar noise is eliminated in the latter version. In addition, the test cases demonstrate that the new shallow-water model maintains the properties of the original GAMIL-SW with respect to numerical accuracy and computational stability. This study helps to identify appropriate governing equations to further develop the next generation of GAMIL dynamical core.

Plain Language Summary

The dynamical core describes the atmospheric motion and its thermodynamic state in a forecast model, acting like the engine of car. The dynamical core needs to numerically solve the governing equations, which involves considering various aspects, such as mathematical equations, numerical methods, a spherical grid and so on. Designing a shallow-water model is often the first step in designing a new generation of dynamical core. This paper describes a new shallow-water model with vector-invariant equations that differ from original model. The new model is designed to avoid the polar noise problem found in the original shallow-water model. By comparing the two models, the source of polar noise on the latitude-longitude grid is analyzed. Idealized experiments also demonstrate that the new shallow water model is able to overcome the polar noise problem and maintains the computational performance of the original model.

1 Introduction

Atmospheric general circulation models (AGCMs) are one of the crucial tools for operational numerical weather prediction and climate modeling, and are one of the fundamental components in Earth system models (ESMs) (Wang et al., 2009). At the heart of AGCMs is the dynamical core, which is responsible for solving the governing equations of atmospheric dynamics and thermodynamics on the resolved scales (Thuburn, 2008). Along with the advances in high-performance computing, substantial investments are being made in the development of the next generation of global non-hydrostatic high-resolution numerical models at modeling centers around the world (e.g., Skamarock et al., 2012; Satoh et al., 2014; Ullrich et al., 2017; Kühnlein et al., 2019). The Grid-point Atmospheric Model of IAP LASG (GAMIL) is an AGCM based on the finite-difference scheme, developed by the State Key Laboratory of Numerical Modeling for Atmospheric Sciences and Geophysical Fluid Dynamics (LASG) in the Institute of Atmospheric Physics (IAP) of the Chinese Academy of Sciences (Wang et al., 2004; Wang & Ji, 2006). GAMIL is the atmospheric component in the coupled climate system model FGOALS-g (Flexible Global Ocean-Atmosphere-Land System model: grid-point version) (e.g., Yu et al., 2008; L. Li et al., 2013). However, as this model remains to solve the hydrostatic primitive equations, it is urgent to upgrade the model to a non-hydrostatic version for higher-resolution global weather forecast and climate modeling. In general, in the process of developing atmospheric models, model developers tend to start from the shallow-water equations, as they mimic the important features of the horizontal aspects of the dynamics (e.g., Thuburn, 2008; Thuburn & Cotter, 2012; Staniforth & Thuburn, 2012). Many formulations of the shallow-water equations on a rotating sphere are available. These for-

65 mulations are equivalent in the continuous case but lead to very different discretization
 66 forms. Moreover, the shallow-water equations have five basic conservative integrals, in-
 67 cluding three primary integrals (total mass, total absolute angular momentum and to-
 68 tal potential vorticity) and two quadratic integrals (total energy and total potential en-
 69 strophy) (Wang & Ji, 2003). If we want to simulate the continuous adiabatic friction-
 70 less governing equations faithfully, numerical methods should be applied to approximately
 71 conserve these integrals, particularly the quadratic ones, which is the necessary condi-
 72 tion for avoiding computational instability in a nonlinear system (Sadourny, 1975; Arakawa
 73 & Lamb, 1977, 1981).

74 GAMIL uses the IAP variable transformation method (Zeng & Zhang, 1987; Zeng
 75 et al., 1989; Zhang, 1990) to convert the standard primitive equations to the quadratic
 76 conservation form, which ensures the conservation of total effective energy in the hydro-
 77 static model under spatial finite-difference discretization. The single-layer shallow-water
 78 version of GAMIL (GAMIL-SW) has many of the same properties as its hydrostatic ver-
 79 sion, such as anti-symmetric spatial operators, and total mass and total energy conser-
 80 vation. Consequently, various idealized test cases for the shallow-water model (e.g., Mc-
 81 Donald & Bates, 1989; Williamson et al., 1992; Bates & Li, 1997; Galewsk et al., 2004;
 82 Nair et al., 2005; Shamir & Paldor, 2016; Ferguson et al., 2019) can be applied to eval-
 83 uate the basic numerical schemes from multiple perspectives, for example, the model grid,
 84 prognostic equations, variable placement and numerical method. Williamson et al. (1992)
 85 proposed a standard suite of test cases for verifying numerical algorithms for solving the
 86 shallow-water equations on a sphere. We evaluated GAMIL-SW with the test case 5 of
 87 the suite and found that the polar noise is noticeable in this case. The unphysical noise
 88 is at the grid scale and propagates from the poles to the mid-latitudes. The noisy so-
 89 lution is likely to be detrimental in three-dimensional simulations when the physical pro-
 90 cesses are coupled within the dynamical core, for example, via advection and wave prop-
 91 agation. Therefore, this problem is critical and needs to be solved by designing suitable
 92 numerical methods for the dynamical core.

93 The objective of this study is to analyze the polar noise and provide a solution to
 94 the problem. A number of approaches have been attempted without success. The ma-
 95 jor efforts in the early phase are in twofold. First, averaging in the calculation of Cori-
 96 olis terms due to the use of the Arakawa-C staggered grid was suspected, which may lead
 97 to grid-scale oscillations when the Rossby deformational radius is under-resolved, but
 98 this is not the case for the model resolution in this study. Second, we endeavored to add
 99 artificial diffusion or damping, a polar fast Fourier transform filter, a digital filter or a
 100 nonlinear diffusion to remove the noise. However, none of these approaches have been
 101 found to be effective. Nevertheless, during the investigations, two features were noticed.
 102 One is that the noise disappears when the nonlinear momentum advection terms are switched
 103 off, and the other is that the abrupt increase of the potential enstrophy may result from
 104 the noise. Therefore, the source of the noise is probably related to these two phenom-
 105 ena. On the basis of these observations, we turn to the vector-invariant form of the hor-
 106 izontal momentum equation, which bypasses the potential problematic discretization of
 107 nonlinear horizontal momentum transport (Skamarock et al., 2012). In addition, the spa-
 108 tial discretization can be designed to dissipate the potential enstrophy (i.e., the square
 109 of the potential vorticity) without violating the total energy conservation (Ringler et al.,
 110 2010).

111 The remainder of this paper is organized as follows. Section 2 introduces the shallow-
 112 water equations in vector-invariant form, and the spatial discretization of the equations
 113 on the latitude-longitude (lat-lon) grid is described in detail in section 3. Section 4 dis-
 114 cusses the polar noise in the numerical experiments, and section 5 provides a summary
 115 and conclusion.

2 The shallow-water equations in vector-invariant form

The standard nonlinear shallow-water equations, including the mass continuity equation in flux form and momentum equation in advection form, can be expressed in vector form as

$$\frac{\partial h}{\partial t} + \nabla \cdot (h\mathbf{u}) = 0 \quad (1)$$

$$\frac{\partial \mathbf{u}}{\partial t} + \mathbf{u} \cdot \nabla \mathbf{u} + f\mathbf{k} \times \mathbf{u} = -g\nabla(h + h_s) \quad (2)$$

where h is the fluid thickness, \mathbf{u} is the fluid velocity vector with components u and v in the longitudinal (λ) and latitudinal (φ) directions, respectively, and \mathbf{k} is the local unit vertical vector. The other three parameters are the Coriolis parameter $f = 2\Omega \sin \varphi$, gravity acceleration g , and bottom topography h_s , in which Ω is the rotation rate of the Earth. The momentum advection term can be reformulated into a vector-invariant form by the so-called Lamb transformation (e.g., Gassmann & Herzog, 2008; Zängl et al., 2015)

$$\mathbf{u} \cdot \nabla \mathbf{u} = \xi \mathbf{k} \times \mathbf{u} + \nabla \left(\frac{1}{2} \mathbf{u}^2 \right) \quad (3)$$

There are two ways to write the vorticity terms

$$(\xi + f)\mathbf{k} \times \mathbf{u} \quad \text{and} \quad q\mathbf{k} \times h\mathbf{u} \quad (4)$$

where $q = (f + \xi)/h$ is the potential vorticity (PV), defined as the ratio between the absolute vorticity and the fluid thickness, and $\xi = \mathbf{k} \cdot (\nabla \times \mathbf{u})$ is the relative vorticity. As in Peixoto et al. (2018), the two vorticity terms can be referred to as the non-depth-weighted form and depth-weighted form, respectively. They are equivalent in the continuous form, but are different for discretization. The depth-weighted form is flexible for designing a numerical scheme of potential enstrophy conservation or dissipation by introducing the PV (e.g., Sadourny, 1975; Burridge & Haseler, 1977; Arakawa & Lamb, 1981; Takano & Wurtele, 1982; Arakawa & Hsu, 1990; Ringler et al., 2010). The non-depth-weighted form has been studied in some shallow-water models (e.g., Lin & Rood, 1997; Tomita et al., 2001; Ringler & Randall, 2002; Wang & Ji, 2003; Bonaventura & Ringler, 2005) and adopted in certain baroclinic models (e.g., Lin, 2004; Skamarock et al., 2012; Zängl et al., 2015). In this study, the depth-weighted form is used in the new shallow-water model.

By substitution, the vector-invariant form of the momentum equation can be written as:

$$\frac{\partial \mathbf{u}}{\partial t} + qh\mathbf{u}^\perp + \nabla K = -g\nabla(h + h_s) \quad (5)$$

where $K = \mathbf{u}^2/2$ denotes the horizontal kinetic energy. $h\mathbf{u}$ and $h\mathbf{u}^\perp = h\mathbf{k} \times \mathbf{u}$ denote the normal and tangential mass flux, respectively. The second term in the momentum equation (Equation (5)) involving q does not contribute to the change of total kinetic energy and is also known as the nonlinear PV flux or nonlinear Coriolis force. Through this term, potential enstrophy can be damped by employing a diffusive advection scheme for PV, such as the anticipated potential vorticity method (APVM) or the scale-selective dissipation method (Sadourny & Basdevant, 1985; Q. Chen et al., 2011).

Thuburn et al. (2009) and Ringler et al. (2010) discussed at length a finite-volume approach used to model the shallow-water system on arbitrarily structured grid. In Thuburn et al. (2009), the linearized version of continuity equation (Equation (1)) and momentum equation (Equation (5)) was analyzed to derive a numerical method, called TRISK (Thuburn & Cotter, 2012), mainly for the discretization of the Coriolis term on an arbitrarily structured orthogonal C-grid, which allows for representation of the stationary geostrophic modes in the linearized equations. The main result of Thuburn et al. (2009) is a set of weights for diagnosing the tangential velocity from the surrounding normal

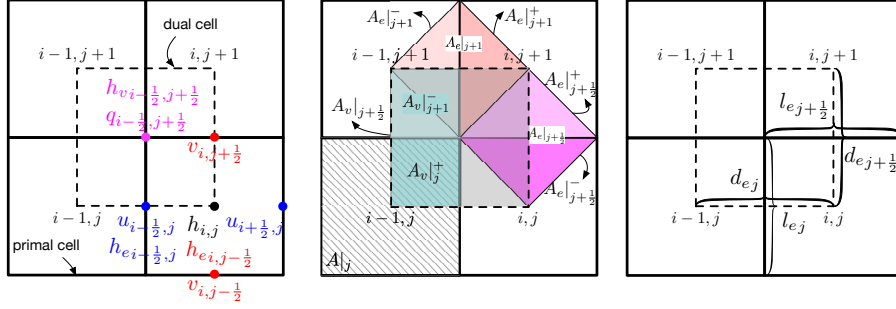


Figure 1. Definition of elements in C-grid staggering on the lat-lon grid. i and j are the index in the zonal and meridional direction over the primal cell, respectively. The primal cell (solid) and the dual cell (dashed) are orthogonal, that is, the edges of primal cell are orthogonal to the edges of dual cell. The areas of primal cell and dual cell are $A|_j$ and $A_v|_{j+\frac{1}{2}}$, respectively. $A_v|_j^+$ ($A_v|_{j+1}^-$) is the overlapping area between the primal and dual cells, and $A_e|_{j+1}$ ($A_e|_{j+\frac{1}{2}}$) is the unique area associated with each edge e , which is the sum of two triangles on either side of the edge. All areas A and edge lengths l_e are calculated in the spherical geometry, and the distance between neighboring cells is set by $d_e = 2A_e/l_e$.

velocities. Ringler et al. (2010) further extended the TRiSK method to the nonlinear shallow-water equations on the spherical centroidal Voronoi tessellation (SCVT) mesh and formulated a spatial discretization that conserves the total energy and potential vorticity, as well as conserves or dissipates the potential enstrophy. Weller et al. (2012) investigated five quasi-uniform spherical grids by using the same TRiSK method to solve the shallow-water equations. However, although the TRiSK method is applicable to a wide variety of meshes theoretically, previous studies have utilized only quasi-uniform meshes, and the numerical accuracy of the method degrades to only first-order due to some unwanted features of those grids, for example, the dual edges do not bisect the primary edges perpendicularly, and there are several pentagon cells different from the surrounding hexagon cells (e.g., Ringler et al., 2010; Skamarock et al., 2012; Weller et al., 2012). Motivated by these considerations, in this study, the shallow-water model in vector-invariant form is pursued on the regular lat-lon grid to solve the polar noise problem and achieve second-order accuracy.

3 Spatial discretization of equations

The Arakawa-C grid has good dispersion properties of the inertia-gravity wave and gives an accurate representation of the geostrophic adjustment process provided the radius of deformation is well resolved (Arakawa & Lamb, 1977). The prognostic variables are discretized with the C-grid staggering as illustrated in Figure 1. The horizontal velocity normal to the cell edge (u and v) as a point-wise value is prognosed at the cell edges. The thickness field $h_{i,j}$ as a cell-averaged value is prognosed at the primal cell centers (i, j). All vorticity-related variables, including relative vorticity ($\xi_{i-\frac{1}{2}, j+\frac{1}{2}}$), thickness ($h_{vi-\frac{1}{2}, j+\frac{1}{2}}$) and potential vorticity ($q_{i-\frac{1}{2}, j+\frac{1}{2}}$), are diagnosed or mapped from prognostic variables on the primal cell. In view of computational efficiency, all the time-independent values, including area, length, and distance, are pre-calculated and stored before the time integration begins. The spatial discretization is a mixed finite-volume/finite-difference scheme, and the main calculations are described in the following subsections.

3.1 Divergence operator

For the continuity equation (Equation (1)) in flux form, the divergence of mass flux can be simply discretized using the Gauss divergence theorem over a primal cell:

$$\nabla \cdot (h\mathbf{u})_{i,j} = \frac{1}{A|_j} \sum_{e \in (i,j)} \hat{h}_e u_e l_e \quad (6)$$

where u_e represents either u or v component of velocity at the edge point and positive flux is outward, $A|_j$ and l_e denote the area and the edge length of the primal cell, respectively. The thickness at the cell edge \hat{h}_e needs to be interpolated from the primal cell centers. The velocity divergence operator has second-order accuracy on the lat-lon grid because the velocity is centered on the primal cell edge, which is not likely the case for the Voronoi mesh. As a result, the accuracy of the mass flux divergence operator is determined by the interpolation approximation of the thickness at the cell edge. Midpoint interpolation $\hat{h}_e = \frac{h_i + h_{i+1}}{2}$ is used on a Voronoi grid in Ringler et al. (2010), i.e., the edge weight is 1/2. It has second-order accuracy because the edges bisect the lines between the Voronoi generating points.

However, the midpoint scheme decreases the interpolation accuracy for the edge thickness on the lat-lon grid. The edge weight used for the interpolation is not equal in the zonal and meridional directions. In the zonal direction, the two triangles at the west and east side of one longitude line are symmetric and equal to each other, for example, $A_e|_{j+1}^+$ is equal to $A_e|_{j+1}^-$. However, in the meridional direction, the area of the rectangular mesh changes with respect to latitude, thus the two areas at the north and south side of one latitude line are not equal, for example, $A_e|_{j+\frac{1}{2}}^+$ is not equal to $A_e|_{j+\frac{1}{2}}^-$. Given the triangular area as weight, Weller et al. (2012) proposed an alternative interpolation for the non-Voronoi grid, which ensures the second-order accuracy of conservative mapping between primal and dual meshes. For example, in Figure 1

$$\hat{h}_{ei,j+\frac{1}{2}} = \frac{A_e|_{j+\frac{1}{2}}^+ h_{i,j+1} + A_e|_{j+\frac{1}{2}}^- h_{i,j}}{A_e|_{j+\frac{1}{2}}} \quad (7)$$

$A_e|_{j+\frac{1}{2}}^+$ and $A_e|_{j+\frac{1}{2}}^-$ are the triangular areas at the north and south of the edge with $A_e|_{j+\frac{1}{2}} = A_e|_{j+\frac{1}{2}}^+ + A_e|_{j+\frac{1}{2}}^-$. In addition, it should be noted that the two triangles in the zonal direction of one cell are exactly spherical triangles because each edge of the triangle is one part of a great circle line, for example, $A_e|_{j+1}^-$ and $A_e|_{j+1}^+$, but the two triangles in the meridional direction of one cell are not spherical triangles because one edge of the triangle is part of the latitude line that is not a great circle except the Equator, for example $A_e|_{j+\frac{1}{2}}^-$ and $A_e|_{j+\frac{1}{2}}^+$. Thus, care must be taken to calculate the area of triangles in the spherical geometry on the lat-lon grid.

3.2 Discretization of normal gradient

In the momentum equation (Equation (5)), to calculate $\partial \mathbf{u} / \partial t$ one needs to discretize the gradient of kinetic energy and geopotential on the cell edge. On the lat-lon grid, the edge of the primal cell is perpendicular to and bisected by the edge of the dual cell; hence, the second-order central finite-difference method can be implemented straightforwardly. For example, on the edge point $(i - \frac{1}{2}, j)$, the gradient of geopotential in the zonal direction is calculated as

$$\nabla h \cdot \mathbf{n}_e = \frac{h_{i+1,j} - h_{i,j}}{d_{ej}} \quad (8)$$

where \mathbf{n}_e is the normal direction to edge e and d_{ej} is the zonal distance between $h_{i,j}$ and $h_{i+1,j}$. This simple two-point central finite-difference on the lat-lon grid ensures that the gradient has second-order accuracy and is curl free around vertices.

3.3 Discretization of potential vorticity

In the momentum equation (Equation (5)), to calculate $\partial \mathbf{u} / \partial t$ one needs to interpolate q , h , and \mathbf{u}^\perp onto the \mathbf{u} grid. This subsection describes the interpolation of q and h ; how to calculate the tangential \mathbf{u}^\perp is to be described in subsection 3.6. PV is defined as absolute vorticity divided by the thickness within the shallow-water model. On the staggered C-grid, it can be calculated at either the primal cell center where thickness is located or the dual cell center where relative vorticity is naturally calculated by applying the circulation theorem to the surrounding u and v . Lin and Rood (1997) defined PV on the primal cell to ensure that PV is accompanied by a valid thickness equation. Sadourny (1975), Arakawa and Lamb (1981) and Ringler et al. (2010) defined PV on the dual cell instead of the primal cell to obtain the PV properties of compatibility and consistency. To avoid the creation of a null space in the divergence field (Skamarock, 2008; Ringler et al., 2010), we define PV on the dual cell center. First, the relative vorticity is discretized by applying Stokes' circulation theorem over a dual cell:

$$\xi = \mathbf{k} \cdot (\nabla \times \mathbf{u}) = \frac{1}{A_v} \sum_{e \in EV(v)} u_e d_e \quad (9)$$

where A_v denotes the area of one dual cell, $e \in EV(v)$ denotes all edges of one dual cell, u_e represents either u or v of velocity circulating one dual cell, and positive circulation is anticlockwise. d_e is the edge length of the dual cell. Second, thickness h_v on the primal vertex needs to be interpolated from the surrounding cell centers; therefore, equation (25) in Ringler et al. (2010) is applied. For example, in Figure 1

$$h_{vi-\frac{1}{2},j+\frac{1}{2}} = \frac{1}{A_v|_{j+\frac{1}{2}}} [A_v|_j^+ (h_{i-1,j} + h_{i,j}) + A_v|_{j+1}^- (h_{i-1,j+1} + h_{i,j+1})] \quad (10)$$

On the lat-lon grid, the overlapping area between the primal and dual cells is equal in the zonal direction, thus the same area weight $A_v|_j^+$ is used for both $h_{i-1,j}$ and $h_{i,j}$, and the same area weight $A_v|_{j+1}^-$ is used for both $h_{i-1,j+1}$ and $h_{i,j+1}$. Moreover, the area of the primal cell, dual cell, and the intersection are accurate calculations rather than approximate ones in spherical geometry. Consequently, the sum of four overlapping areas in one primal cell is exactly equal to the area of the primal cell, and the sum of four overlapping areas in one dual cell is exactly equal to the area of the dual cell. As a result, this interpolation scheme ensures that the divergence field on the dual mesh is compatible with the divergence field on the primal cell. In addition, on the lat-lon grid, the thickness over the primal and dual cells is located at the center of the primal and dual cells. These constraints on the lat-lon grid ensure that the interpolation operator has second-order accuracy (Thuburn & Cotter, 2012).

After the calculation of PV on a dual cell, the next step is the interpolation of PV to the edge point from the dual cell for the nonlinear Coriolis force term. Two interpolation algorithms are used in this study. One is the midpoint scheme, which allows for the conservation of potential enstrophy. Another is APVM (Sadourny & Basdevant, 1985; Ringler et al., 2010), which leads to potential enstrophy dissipation as it is an upwind-biased estimate of the edge PV and provides an enstrophy sink.

$$\text{midpoint: } q_e = \frac{q_{v1} + q_{v2}}{2}, \quad (11)$$

$$\text{APVM: } q_e = \frac{q_{v1} + q_{v2}}{2} - \frac{1}{2} \mathbf{u}_e \cdot \nabla_e q \delta t \quad (12)$$

where q_{v1} and q_{v2} are the PV at two ends of one primal edge, $\nabla_e q = (\frac{\partial q}{\partial x}, \frac{\partial q}{\partial y})$ is the gradient of q at edge point and δt is the time step. On the lat-lon grid, for the $u(v)$ point, $\frac{\partial q}{\partial y}(\frac{\partial q}{\partial x})$ can be directly calculated using the two endpoint PVs of one edge with the finite-difference method, while $\frac{\partial q}{\partial x}(\frac{\partial q}{\partial y})$ needs to be interpolated from surrounding values that are calculated on the edge point. The interpolation method is the same as that of tangential velocity described in subsection 3.6. With respect to other kinds of APVM, refer to Weller (2012). In this study, the midpoint and APVM methods are applied.

3.4 Calculation of kinetic energy

In the momentum equation (Equation (5)), if the kinetic energy is defined on the primal cell centers, the calculation of the kinetic gradient has second-order accuracy using the central finite-difference method. The expression of kinetic energy in the discrete system is determined by the constraint of conservative exchange between potential and kinetic energy. Therefore, based on the calculation of thickness on the edge (Equation (7)), where the triangular area either side of each edge is the weight, the kinetic energy in terms of the normal velocities is derived (see Appendix). For example, in Figure 1

$$K_{i,j} = \frac{1}{A|_j} \left(A_e|_{j+\frac{1}{2}}^- v_{i,j+\frac{1}{2}}^2 + A_e|_{j-\frac{1}{2}}^+ v_{i,j-\frac{1}{2}}^2 + A_e|_j^+ u_{i+\frac{1}{2},j}^2 + A_e|_j^- u_{i-\frac{1}{2},j}^2 \right) \quad (13)$$

where $A|_j = A_e|_{j+\frac{1}{2}}^- + A_e|_{j-\frac{1}{2}}^+ + A_e|_j^+ + A_e|_j^-$. This definition is the same as Weller et al. (2012) and more suitable for non-Voronoi grids. There are two points to note for the calculation of kinetic energy on the primal cell. First, the distance between cells is set by $d_e = 2A_e/l_e$ instead of direct calculation in spherical geometry. In other words, the area associated with edge e and the edge length l_e are calculated in spherical geometry before the distance d_e is determined. Second, to ensure energetic consistency, the same area weight must be used for interpolation of thickness from cells to edges.

3.5 Discretization of the nonlinear Coriolis term

One of the requisites for total energy conservation is that the Coriolis force neither creates nor destroys kinetic energy as the Coriolis force is always orthogonal to the velocity vector. Under this constraint, the nonlinear Coriolis force term (or PV flux) is constructed between the target and surrounding edges as follows, exactly as in Ringler et al. (2010)

$$(qhu^\perp)_e = \frac{1}{d_e} \sum_{e' \in ECP(e)} w_{ee'} \ell_{e'} \hat{h}_{e'} u_{e'} \tilde{q}_{ee'} \quad (14)$$

where d_e is the distance between two neighboring primal cells that share edge e , $e' \in ECP(e)$ denotes the four edges (v -grid for qhu and u -grid for qhv) belonging to the two primal cells that share edge e , and $w_{ee'}$ is the interpolation weight, which is specified in subsection 3.6. One symmetric formulation of $\tilde{q}_{ee'}$ is $(\tilde{q}_e + \tilde{q}_{e'})/2$, where $\tilde{q}_e, \tilde{q}_{e'}$ are the PVs at the edge point remapped from PVs at the primal vertices. In this way, the symmetry of the two \tilde{q} terms along with the symmetry of remapping weight $w_{ee'}$ following Thuburn et al. (2009) ensure that the Coriolis term is energy conserving. An alternative non-symmetric formulation of $\tilde{q}_{ee'}$ is q_e , which is directly defined on the edge using an interpolation scheme for the PV. This formulation does not guarantee that the nonlinear Coriolis force is energetically-neutral, but it does give an accurate treatment of PV from a potential enstrophy perspective (Thuburn & Cotter, 2012; Ringler et al., 2010; Thuburn et al., 2014). In this study, the symmetric formulation is applied along with the midpoint (Equation (11)) and APVM schemes (Equation (12)) for the edge PV, which leads to inherent potential enstrophy conservation and dissipation, respectively.

3.6 Calculation of weights and tangential velocity

The weight $w_{ee'}$ used in the previous subsection is a key parameter because it is used to calculate the PV flux as well as the tangential velocities (vector quantities along edges). The weight $w_{ee'}$ is derived from the sum of area fractions for each cell vertex

$$w_{ee'} = \pm \left(\frac{1}{2} - \sum_v \frac{A_{iv}}{A_i} \right) \quad (15)$$

where A_{iv} is the overlapping area between the dual cell around vertex v and the primal cell i , and the vs are the vertices in a walk between edge e and e' . The weights are proportional to the overlap area. For the detailed computational method, refer to Thuburn

et al. (2009) and Weller et al. (2012). As Thuburn et al. (2009) noted, the weight can be set to 1/4 on the lat-lon grid. The two options are provided in the new shallow-water model and the experiment results are similar, thus 1/4 is adopted at present.

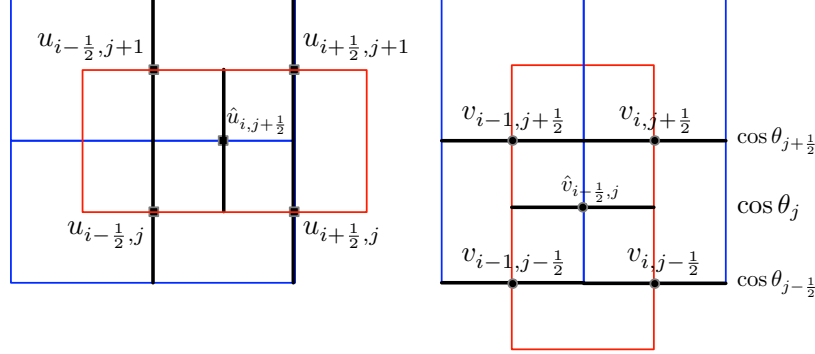


Figure 2. Illustration of reconstruction of tangential velocity at the edge points. It is obtained using the tangential velocity flux divided by the length across the edge, and the tangential velocity flux at $(i, j + \frac{1}{2})$ and $(i - \frac{1}{2}, j)$ are averaged by using the neighboring four normal velocity fluxes, respectively.

The tangential velocity can be reconstructed from neighboring normal components at the edges of the cells. The interpolation needs to ensure that the divergence of vector field on the dual cell is a convex combination of the divergence on the primal cell:

$$u_e^\perp = \frac{1}{d_e} \sum_{e' \in ECP(e)} w_{ee'} l_{e'} u_{e'} \quad (16)$$

where $u_{e'}$ denotes the normal velocity. Specifying the interpolation operator on the lat-lon grid, Figure 2 illustrates how to interpolate neighboring normal wind components (u and v) to the tangential wind components (\hat{u} and \hat{v}). With respect to the velocity flux and spherical coordinates, the tangential velocity flux is averaged by the surrounding four normal velocity fluxes, for example, as given by equation (17) and (18). By derivation, \hat{u} is the four-point arithmetic mean from surrounding u s, but for \hat{v} , the interpolation needs to contain geometrical factors ($\cos \varphi$) due to grid intervals varying with latitude. The tangential velocity is calculated as follows

$$a \Delta \varphi \hat{u}_{i, j+1/2} = \frac{1}{4} (a \Delta \varphi u_{i-1/2, j+1} + a \Delta \varphi u_{i-1/2, j} + a \Delta \varphi u_{i+1/2, j+1} + a \Delta \varphi u_{i+1/2, j}) \quad (17)$$

$$a \cos \varphi_j \hat{v}_{i+1/2, j} = \frac{1}{4} (a \cos \varphi_{j+1/2} v_{i-1, j+1/2} + a \cos \varphi_{j-1/2} v_{i-1, j-1/2} + a \cos \varphi_{j+1/2} v_{i, j+1/2} + a \cos \varphi_{j-1/2} v_{i, j-1/2}) \quad (18)$$

and can be simplified as

$$\hat{u} = \overline{u}^{\lambda \varphi} \quad (19)$$

$$\hat{v} = \frac{1}{\cos \varphi} \overline{v \cos \varphi}^{\lambda \varphi} \quad (20)$$

where the overline with superscript indicates an equally weighted two-point average in the spatial direction (λ or φ) on the lat-lon grid (Thuburn & Staniforth, 2004; Thuburn et al., 2009).

3.7 Calculation of potential vorticity on the pole

As the staggered Arakawa C-grid is applied on the lat-lon grid, two different placements of prognostic variables at the poles are available (e.g., Thuburn & Staniforth, 2004), that is, u -at-pole and v -at-pole, as shown in Figure 3ab. These two placements result in different calculation of potential vorticity near the pole. The first placement needs to calculate one circle of PV at half a grid length to the pole, while each relative vorticity is calculated in one small sector by the u and v wind components using Stokes' theorem. The second placement requires calculation of only one value of relative vorticity at the pole with a ring of u values closest to the pole using Stokes' theorem.

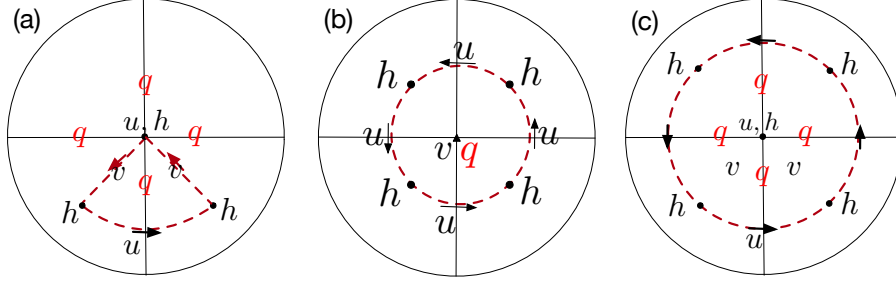


Figure 3. Relative horizontal placement of (a) u -at-pole and (b) v -at-pole and (c) u -at-pole but vorticity next to the pole is calculated using Stokes' theorem used in the new shallow-water model.

Another issue associated with the two variable placements is the size of the time step, because the maximum numerically stable time step for the finite-difference scheme is mostly limited by the zonal grid spacings on the lat-lon grid. Assuming the same Courant-Friedrichs-Lewy (CFL) number, $CFL = c\Delta t/\Delta x$, the time step Δt will become smaller as zonal grid spacing Δx becomes smaller under the condition of the same wave speed c . Therefore, with respect to the time step, the arrangement with v located at the pole is approximately half of that with u -at-pole. For this reason, the u -at-pole is preferred. But in the following tests, it is found that u -at-pole exhibits polar noises as in GAMIL-SW, therefore another PV calculation method is casted which also uses Stokes' theorem on the circle of u as shown in Figure 3c to imitate v -at-pole. In this way, the degree of freedom of relative vorticity is reduced to one as in v -at-pole, which plays a smoothing role on the PVs around the pole.

4 Analysis of polar noise and assessment of the new shallow-water model

The spatial discretization of the vector-invariant form of the equations on the lat-lon grid is described in the previous section. Another important part is the temporal discretization scheme in the evolution equations. In the following numerical experiments, the explicit second-order predictor-corrector method (Wang & Ji, 2006) is applied. The full discretized equations can be written in the following form:

$$\frac{F^{n+1} - F^n}{\Delta t} = LF \quad (21)$$

where $F = u, v, h$, and L denotes the discrete spatial operator; thus, LF denotes the explicit time tendency. To solve the above equation, the predictor-corrector method needs three iterative calculations, including one predictor substep and two corrector substeps:

$$F^* = F^n + \frac{\Delta t}{2} LF^n \quad (\text{predictor}) \quad (22)$$

$$F^{**} = F^n + \frac{\Delta t}{2} L F^* \quad (\text{the first corrector}) \quad (23)$$

$$F^{n+1} = F^n + \Delta t L F^{**} \quad (\text{the second corrector}) \quad (24)$$

The first two substeps in the predictor-corrector integrator update the state from time level n to an intermediate time level, and the last substep obtains the state at the next time level $n + 1$.

In addition, as in Williamson et al. (1992), numerical errors are estimated quantitatively by using two norm and infinity norm defined by

$$\ell_2(h) = \frac{\left\{ I \left[(h(\lambda, \varphi) - h_t(\lambda, \varphi))^2 \right] \right\}^{1/2}}{\left\{ I [h_t(\lambda, \varphi)^2] \right\}^{1/2}} \quad (25)$$

$$\ell_\infty(h) = \frac{\max |h(\lambda, \varphi) - h_t(\lambda, \varphi)|}{\max |h_t(\lambda, \varphi)|} \quad (26)$$

where λ and φ are the longitude and latitude of the grid points, respectively, h is the model output, h_t is the true solution if there is an analytic solution or a reference solution and I is a discrete approximation to the global integral

$$I(h) = \int_0^{2\pi} \int_{-\frac{\pi}{2}}^{\frac{\pi}{2}} h(\lambda, \varphi) a \cos \varphi d\varphi d\lambda \quad (27)$$

In addition, when an analytic solution is not available, the simulation calculated by the National Center for Atmospheric Research (NCAR) Spectral Transform Shallow Water Model (Hack & R.Jakob, 1992; Worley & Toonen, 1995) is used for comparison.

4.1 Zonal flow over an isolated mountain

Test case 5 of Williamson et al. (1992) describes a zonal flow impinging on an isolated mountain with a conical shape. The surface or mountain height h_s is given by $h_s = h_{s0}(1 - r/R)$, where $h_{s0} = 2000$ m, $R = \pi/9$, and $r^2 = \min[R^2, (\lambda - \lambda_c)^2 + (\varphi - \varphi_c)^2]$. The center of the mountain is located at $\lambda_c = 3\pi/2$, $\varphi_c = \pi/6$. The wind velocity and height field are similar to the steady-state geostrophic flow test case in subsection 4.4, except $\alpha = 0$, $h_0 = 5960$ m and $u_0 = 20$ m s⁻¹. The initial steady shear-free westerly flow is in geostrophic balance with the geopotential height. As the flow impinges on the mountain, an imbalance between the Coriolis force and the pressure gradient is induced, generating large-amplitude inertia-gravity waves and Rossby waves. After 15 days of simulation, these waves spread around the globe (including the poles). The interaction between the sole forcing orography and the zonal flow lead to strong nonlinearity (e.g., Ringler et al., 2011), which is particularly appropriate for assessing the effectiveness of the numerical method in conserving integral invariants, such as total mass, total energy and total potential enstrophy (e.g., Nair et al., 2005).

First, the geopotential height and the zonal velocity component simulated by GAMIL-SW at day 20 are shown in Figure 4. Observing the animation of the u , the grid-scale noise propagates out from the North Pole. Moreover, the propagation is in the meridional direction, which could not be filtered by the fast Fourier transform filter. There is, however, no noise in the geopotential height field during the same simulation. The evidence suggests that the wind field is more sensitive than the height field, which is probably due to their different time tendencies. If the nonlinear momentum advection terms are switched off, the noise disappears in the wind field. This implies that the nonlinear momentum advection terms have an important role in the presence of noise. Second, as shown in Figure 5, the potential enstrophy increases abruptly when the waves arrive at the poles where the grid-scale noise appears, even if the global total energy is totally conserved over the 20 simulation days. This demonstrates that energy conservation alone

does not prevent the build-up of grid-scale oscillations, though does help to suppress non-linear instability (Thuburn, 2008). The potential enstrophy is approximately conserved before the presence of the noise, which raises the question of whether the noise can be suppressed by dissipating the potential enstrophy. Hence, for the two considerations, we decided to use the vector-invariant equations. This suite of equations does not explicitly contain the nonlinear momentum advection terms and can be flexibly designed to dissipate potential enstrophy, as described in section 3. Replacing the anti-symmetric equations in the original GAMIL-SW with this suite of equations, the new shallow-water model is developed on the same lat-lon grid.

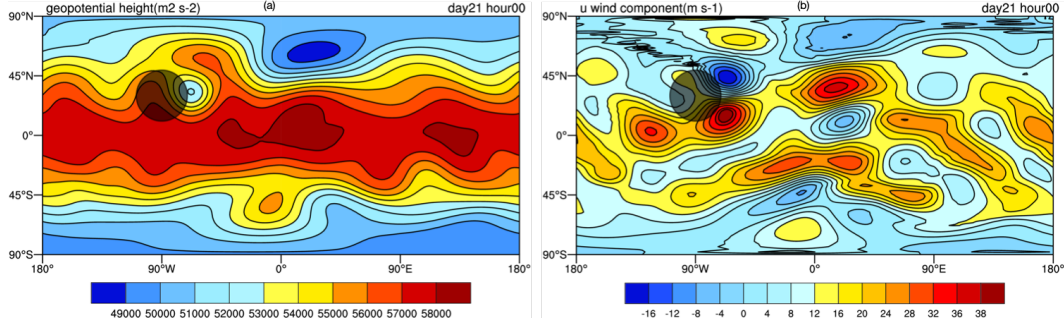


Figure 4. (a) Geopotential height field (contour line spacing is 500 gpm) and (b) zonal velocity component (contour line spacing is 4 m s^{-1}) at day 20 in the zonal flow over an isolated mountain test case simulated by GAMIL-SW. The filled black circle represents the mountain.

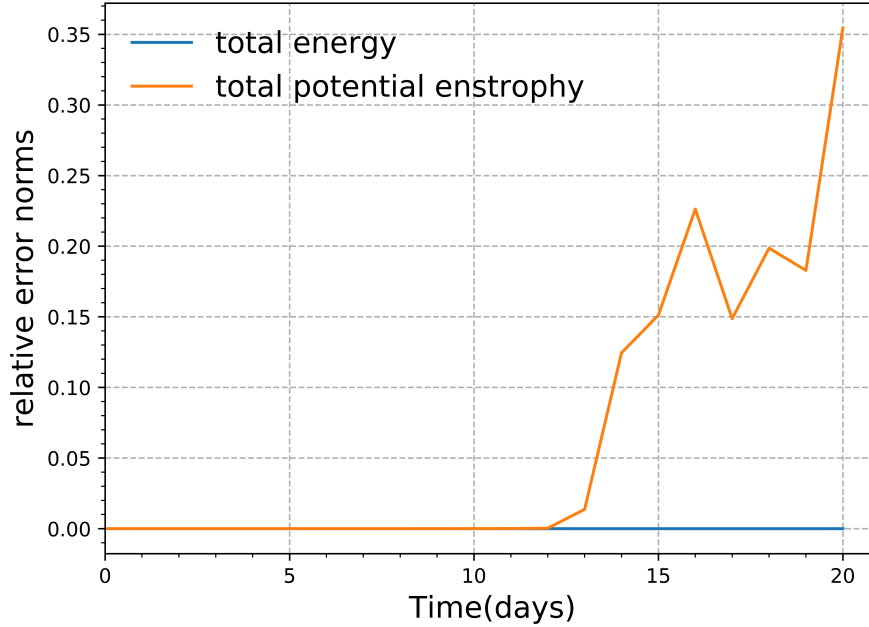


Figure 5. Relative error of global total energy and total potential enstrophy within 20 days of simulation by GAMIL-SW in the zonal flow over an isolated mountain test case.

The simulation results of the new shallow-water model with the two variable placements of u -at-pole and v -at-pole for the same test case are shown in Figure 6. The midpoint scheme for interpolation of PV at the edge points is applied for the two simulations to exclude the influence of dissipation of potential enstrophy. The simulated u wind component with u -at-pole (Figure 6b) shows noise propagating from the pole when the waves arrive at the pole, which is similar to that of GAMIL-SW. This indicates that the nonlinear momentum advection is not the dominant source of polar noise. In contrast, the wind field simulated with the placement of v -at-pole generates no noise at all in the 20 days of simulation (Figure 6a). The numerical schemes implemented in the two simulations are identical except for the variable placement at the pole. Such a difference reveals that the PV or relative vorticity should be well defined at the pole non-singularly (e.g., Lin and Rood, 1997). Figure 6c shows the result simulated with u -at-pole but relative vorticity next to the pole is calculated using Stokes's theorem (Figure 3c). It can be observed that the noises are prohibited to a large extent with this modification. This minor change to the calculation of PVs closet to the pole for u -at-pole results in an unexpected benefit of controlling the noise. Therefore, the noise probably belongs to the trapped modes due to the grid inhomogeneities near the pole on the lat-lon grid (Thuburn, 2013). Further investigation should be conducted to fully reveal the mechanism of this kind of noise.

In addition to not explicitly containing nonlinear momentum advection term, the vector-invariant equation allows for the dissipation of potential enstrophy. To examine the effect of APVM on the noise, the APVM scheme (equation (12)) is adopted in the new shallow-water model with u -at-pole. The simulated pattern of the u wind component (not shown) is almost identical to that of u -at-pole with the midpoint scheme. That is, the dissipation of potential enstrophy does not remove the noise. Moreover, the APVM does not suppress the increase of total potential enstrophy when the noise begins appear, although it does slow down the rate of increase relative to the midpoint scheme, as shown in Figure 7. In addition, as Thuburn et al. (2014) noted, the flow is weakly nonlinear during the first 15 days and the total potential enstrophy should be approximately conserved. However, in this study, the total potential enstrophy begins to increase once the noise is present at day 13. Therefore, the APVM does not have any positive effect on suppressing the noise in this case. The noise should belong to computational modes caused by the numerical scheme rather than the downscale cascade of potential enstrophy physically (e.g., Arakawa & Hsu, 1990; Thuburn, 2008; Thuburn et al., 2014).

4.2 Cross-polar rotating high-low

To further investigate whether the above result is case dependent, the test case proposed by McDonald and Bates (1989) is evaluated, which simulates cross-polar flow with a geostrophically balanced initial state. This test has also been used by Giraldo et al. (2002), Nair et al. (2005) and Jablonowski et al. (2009), for example. The initial condition consists of a height field and the wind field (u, v) derived from the height field via geostrophic relationship. They are given by

$$gh = gh_0 + 2\Omega av_0 \sin^3 \varphi \cos \varphi \sin \lambda \quad (28)$$

$$u = -v_0 \sin \lambda \sin \varphi (4 \cos^2 \varphi - 1) \quad (29)$$

$$v = v_0 \sin^2 \varphi \cos \lambda \quad (30)$$

where $gh_0 = 5.768 \times 10^4 \text{ m}^2 \text{ s}^{-2}$ and $v_0 = 20 \text{ m s}^{-1}$. a and Ω are the radius and rotation rate of the Earth, respectively. It consists of a low and a high, which are symmetrically located on the west and east side of the pole in the Northern Hemisphere (their positions are reversed in the Southern Hemisphere). The low and high rotate in a clockwise direction around the North Pole and deform slightly. They exchange their positions after five days, and the slightly deformed pattern almost returns to the initial location after 10 days of integration. The maximum wind speed is near the pole and exhibits a

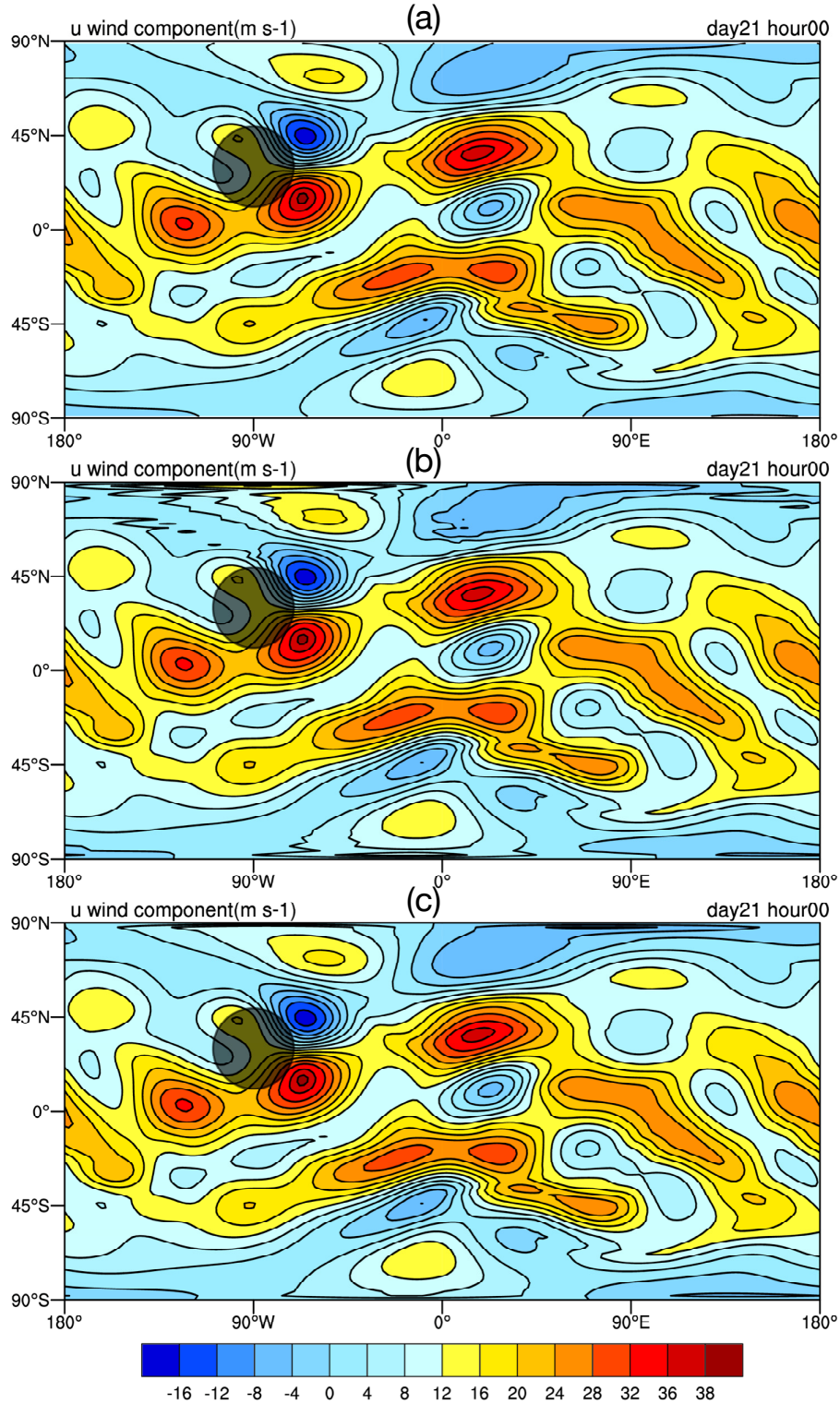


Figure 6. The zonal wind component at day 20 in the zonal flow over an isolated mountain test case with placement of (a) v -at pole, (b) u -at pole without potential enstrophy dissipation and (c) u -at-pole but relative vorticity next to the pole is calculated as a single value using Stokes' theorem. The filled black circle represents the mountain.

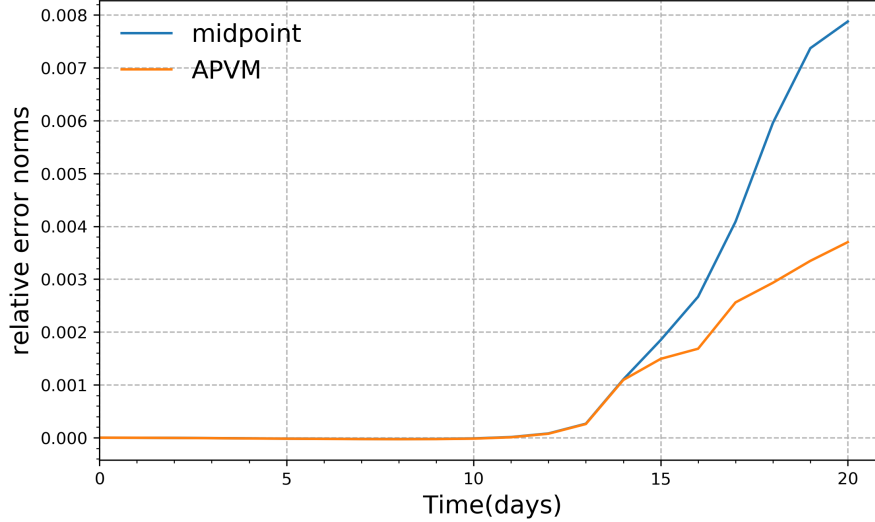


Figure 7. Relative error of global total potential enstrophy within 20 days of simulation using the new shallow-water model with u -at-pole under the midpoint and APVM scheme in the zonal flow over an isolated mountain test case. The increase in total potential enstrophy corresponds to the presence of noise at about day 13.

strong gradient; thereby, this test is well suited for the analysis of polar noise, although this test case has no analytical solution.

The numerical simulations are illustrated in Figure 8, which shows the u wind component at day 10 with different numerical schemes. It can be observed that the GAMIL-SW simulation shows grid-scale noise in the polar domain of about 30° (Figure 8a). Similarly, the new shallow-water model with u -at-pole also shows noise in the polar domain when using the midpoint scheme for interpolation of PV on the edge (Figure 8b), but if the ring of relative vorticity near the pole is calculated using Stokes' theorem, the simulation result (Figure 8c) is almost indistinguishable from the result of v -at-pole (Figure 8d). There are no distortions in the flow pattern with the latter two numerical schemes, and the strong gradient near the pole can be well simulated at the same time. Moreover, the APVM dissipation of potential enstrophy is applied but the result is nearly identical to that in Figure 8a without any improvement. The result of the v wind field shows the same situation and hence is not shown here. Therefore, this qualitative comparative analysis verifies the conclusion from the previous subsection.

On the basis of the analysis of polar noise in the two previous test cases, the following conclusions are obtained. There are two variable placements on the pole for both GAMIL-SW and the new shallow-water model: u -at-pole and v -at-pole. Both of the two shallow-water models with the u -at-pole configuration exhibit polar noise in the same test cases, which demonstrates that the nonlinear momentum advection term is not the source of polar noise. The new shallow-water model with v -at-pole shows no noise, but that with u -at-pole exhibits polar noise and the noise disappears when the relative vorticity is calculated with one minor modification, which demonstrates that the numerical treatment of relative vorticity or PV on the pole is important for controlling polar noise (e.g., Arakawa & Lamb, 1981; Lin & Rood, 1997). The noise in the new shallow-water model with u -at-pole was not alleviated by dissipation of potential enstrophy, which demonstrates that the noise is not produced from the physical cascade of potential enstrophy as some previous studies have suggested (e.g., Arakawa & Hsu, 1990; Thuburn,

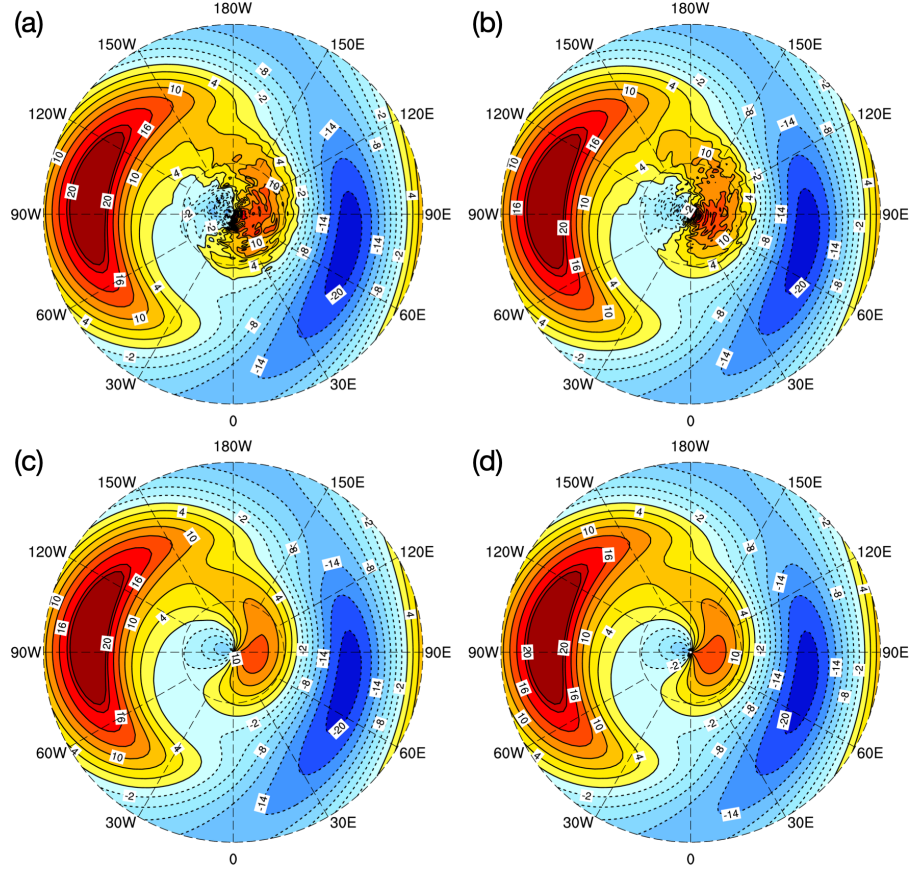


Figure 8. Stereographic projections from the Equator to the North Pole of the zonal wind component at day 10 simulated by (a) GAMIL-SW and by the new shallow-water model with (b) u -at-pole, (c) u -at-pole but relative vorticity next to the pole is calculated using Stokes's theorem and (d) v -at-pole. Contour intervals are 3 m s^{-1} .

2008; Ringler et al., 2010; Thuburn et al., 2014). The new shallow-water model with v -at-pole exhibits no noise, while GAMIL-SW with v -at-pole exhibits noise (figure not shown), which implies that the noise is relevant to the form of equations, numerical schemes, pole problem and so on. Overall, arranging the v velocity component located at the pole may be a good choice, although at the cost of a relatively small time-step size.

4.3 Rossby-Haurwitz wave

The previous two test cases analyzed the numerical polar noise. In the following, the performance of the new shallow-water model is shown in several test cases by comparison with GAMIL-SW or the spectral model. Test case 6 of Williamson et al. (1992) consists of a Rossby-Haurwitz wave of zonal wavenumber 4. This type of wave is an analytic solution for the fully nonlinear non-divergent barotropic vorticity equation on a sphere and has also been widely used to test shallow-water models. Nevertheless, the Rossby-Haurwitz wave is actually unstable as a solution of the shallow-water equations that are analyzed by Thuburn and Li (2000), because small random perturbations in the initial conditions could result in long-term disruption. This was shown to be the case for a wide range of numerical models, including the spectral model, which usually apply diffusion or damping to simulate more stably (e.g., Whitehead et al., 2011; Lauritzen et al., 2011). Moreover, if the model chooses a grid that is not symmetrical across the Equator, the

disruption comes faster. However, the lat-lon grid naturally has the advantage of symmetry across the Equator.

A complete description of the test case is described in detail by Williamson et al. (1992). The initial height field is chosen to be in balance with the velocity field such that the initial velocity field is non-divergent. The minimum fluid height is 8000 m, which occurs at the poles, and the mean fluid height is 9523 m. In addition, the angular velocity of this pattern moving from west to east can be calculated by

$$\nu = \frac{R(3+R)\omega - 2\Omega}{(1+R)(2+R)} \quad (31)$$

where $R = 4$ for the wavenumber, $\omega = 7.848 \times 10^{-6} \text{ s}^{-1}$ and $\Omega = \frac{2\pi}{86400} = 7.272 \times 10^{-5} \text{ s}^{-1}$. With these parameters, the period is approximately 29.36 days for zonal wavenumber 4 of the Rossby-Haurwitz wave. Jakob et al. (1993) questioned how long the initial solution could be expected to remain stable. To address this question, they integrated a T42 model with the time step of 600 s for 60 days, and concluded that a viable numerical method should be able to maintain the wavenumber 4 structure for a minimum of 14 days (Jakob-Chien et al., 1995). However, some studies selected different days for their assessment, such as 60, 14 or 10 days (e.g., Lin & Rood, 1997; Bonaventura & Ringler, 2005; C. Chen & Xiao, 2008; X. Li et al., 2008; Li & Xiao, 2010; Ringler et al., 2010).

Figure 9 presents the height field after simulating three periods (88 days) using the spectral model, GAMIL-SW, and the new shallow-water model, respectively. The solution of the spectral transform method can be considered as the reference solution because the initial flow field can be exactly represented by the basic functions that are spherical harmonics (Lin & Rood, 1997). In fact, GAMIL-SW is able to maintain the basic pattern for as long as 100 days, and the new shallow-water model is also able to reach this level under certain conditions. Here, no attempt is made to obtain the longest simulation time because the spectral model maintains the wave for the longest time. Compared to the reference solution, both the new shallow-water model and GAMIL-SW simulate steadily for three periods, and the results are remarkably similar to the reference solution, both in phase and amplitude, which demonstrates that the new shallow-water model maintains the computational performance of GAMIL-SW in this test case. Moreover, when the same equation and numerical schemes are applied on a SCVT grid symmetrical with the Equator, the model is only able to accomplish the simulation without deformation for about 40 days (Figure 9d). Therefore, in terms of this test case, the lat-lon grid has a natural advantage for simulating the zonally balance flow. This is also one of the main reasons why we still choose the lat-lon grid when design new dynamical core.

4.4 Steady-state geostrophic flow

Test case 2 of the standard shallow-water suite of Williamson et al. (1992) consists of a steady-state nonlinear zonal geostrophic flow. This test case measures the ability of the numerical scheme to maintain a large-scale geostrophic balance, which is an important property of any numerical model for the atmosphere or ocean. Since an analytical solution is available, the mesh convergence rate can be calculated by applying different spatial resolutions. The initial conditions of the fluid depth and the eastward and northward components of velocity at longitude λ and latitude φ are

$$gh = gh_0 - \frac{u_0}{2}(2a\Omega + u_0)(\sin \varphi \cos \alpha - \cos \lambda \cos \varphi \sin \alpha)^2 \quad (32)$$

$$u = u_0(\cos \varphi \cos \alpha + \cos \lambda \sin \varphi \sin \alpha) \quad (33)$$

$$v = -u_0 \sin \lambda \sin \alpha \quad (34)$$

where $gh_0 = 2.94 \times 10^4 \text{ m}^2 \text{ s}^{-2}$ and $u_0 = 2\pi a/(86400 \times 12) \text{ m s}^{-1}$. The Coriolis parameter is

$$f = 2\Omega(\sin \varphi \cos \alpha - \cos \lambda \cos \varphi \sin \alpha) \quad (35)$$

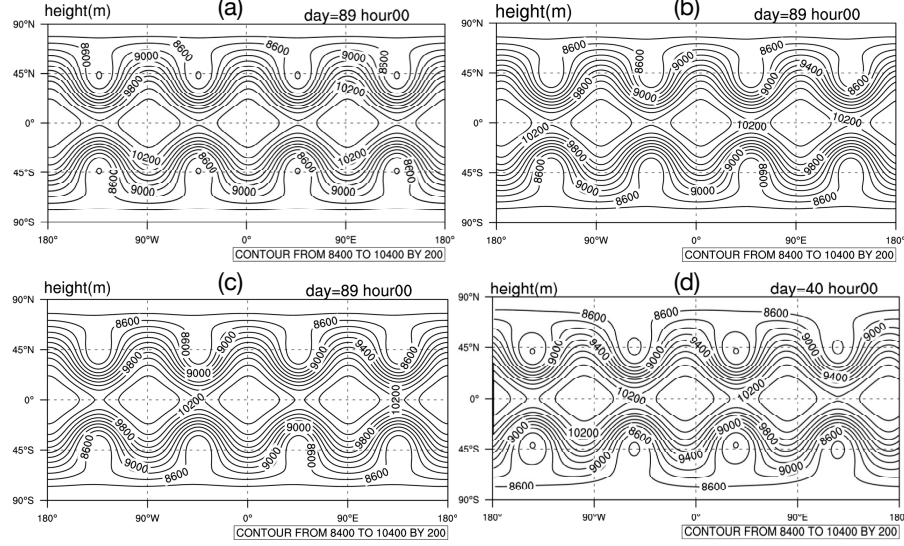


Figure 9. The height field simulated by (a) spectral model, (b) GAMIL-SW and (c) the new shallow-water model at day 89, and (d) the vector-invariant form on a symmetrical SCVT grid at day 40.

The parameter α is the angle between the axis of the flow orientation and the polar axis of the Earth sphere. We analyze here only the results with $\alpha = 0$.

The ℓ_2 and ℓ_∞ error norms calculated with the thickness field of the simulation after 5 days by GAMIL-SW and the new shallow-water model are shown in Figure 10. The spatial resolutions are 2° , 1° , 0.5° and 0.25° , and the corresponding time steps for the simulation are 240 s, 120 s, 60 s, and 30 s, respectively. In this test case with $\alpha = 0$, the APVM scheme is equal to the midpoint scheme because the second term in the APVM will vanish because \mathbf{u}_e and $\nabla_e q$ are perpendicular (Ringler et al., 2010). It can be observed that for resolution higher than 1° , both ℓ_2 and ℓ_∞ error norms of the two models converge with second-order accuracy and the convergence rate increases with increasing resolution. Comparing the error norms at the same resolution, the new shallow-water model generates smaller errors than GAMIL-SW. Moreover, with respect to the convergence rate, the vector-invariant equations on the lat-lon grid are better than the similar equations and numerical method implemented on other unstructured grid, such as SCVT (Ringler et al., 2010). This suggests that the new shallow-water model meets the aim of achieving second-order accuracy. In addition, the low height field error also shows that the new shallow-water model maintains large-scale balance and has steady geostrophic modes without grid-scale oscillations, which is another proof that the lat-lon grid with physically perfect zonal symmetry is in favor of being computationally free of grid-scale oscillations for this kind of zonally flow.

4.5 Barotropically unstable zonal jet

The last test case to be discussed concerns the growth of rapid barotropic instability from a mid-latitude jet, in which the initial wind is zonally symmetric (see Galewski et al., 2004, for detailed numerical description). Simulating the barotropically unstable jet with an initial small-amplitude perturbation is a challenging task for a quasi-uniform grid. As the jet is fast and narrow, numerical truncation errors arising from the misalignment of the jet with the grid would lead to perturbations that also produce instability in a similar manner to the initial perturbation (e.g., C. Chen & Xiao, 2008; Ringler et

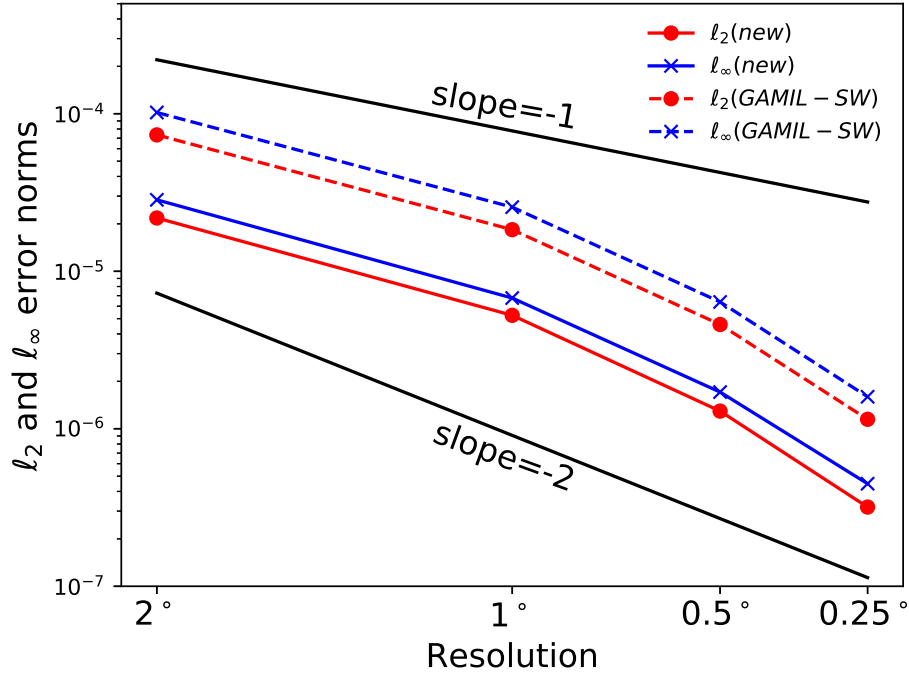


Figure 10. Convergence rate of steady-state geostrophic flow as measured by the l_2 and l_∞ norms based on the geopotential height. Norms of solid and dashed lines are computed by the new shallow-water model and GAMIL-SW with respect to the analytic solution at day 5, respectively. Lines of slope=-1(-2) represents the first- and second-order convergence rates, respectively.

al., 2011; Weller et al., 2012). Therefore, the shallow-water model with a quasi-uniform grid generally needs higher resolution than the previous test cases to reduce the numerical truncation errors (e.g., Ii & Xiao, 2010; Thuburn et al., 2014). For the lat-lon grid, the numerical truncation errors are relatively small because the jet is essentially aligned with the grid. However, since the maximum velocity is around 80 m s^{-1} and the explicit time integration step is restricted by the pole problem of the lat-lon grid as well as there being no polar filter or other treatments at present, only the simulations of low spatial resolution 1° are shown. The vorticity field at different stages simulated by GAMIL-SW and the new shallow-water model with the same resolution are shown in Figure 11. Compared with Figure 4 in Galewsk et al. (2004) that simulated using the spectral model without diffusion, the envelope of the growing barotropic instability of the two models performs essentially identical to the reference. The dominant ridge-trough-ridge pattern with the same amplitude and phase are present in the two simulations.

5 Summary and conclusion

We have analyzed the polar noise found in the barotropic shallow-water version of GAMIL (GAMIL-SW) and provided a solution to the problem. A global mixed finite-volume/finite-difference shallow-water model with the vector-invariant equations on the same lat-lon grid is developed and evaluated, which is designed to maintain conservation of total mass and total energy like GAMIL-SW and, in addition, to be able to conserve potential vorticity and allows for the conservation or dissipation of potential enstrophy.

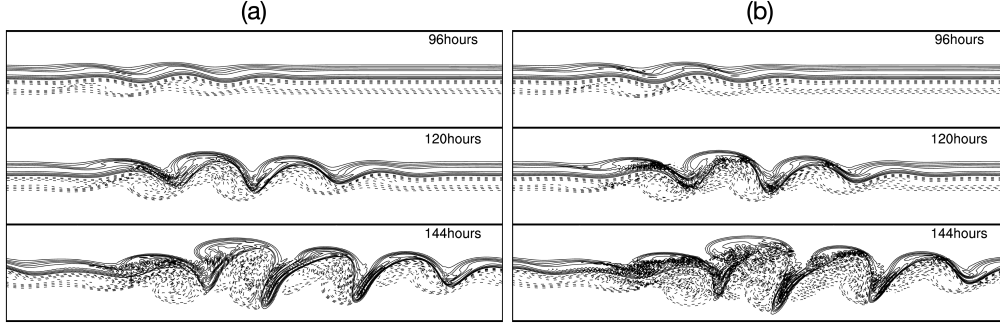


Figure 11. The time evolution of the relative vorticity field for the barotropically unstable zonal jet, simulated by (a) GAMIL-SW and (b) the new shallow-water model. Each panel is 10°N to 80°N, 0° to 360° longitude centered at 90°. The contour interval is $2 \times 10^{-5} \text{ s}^{-1}$, negative contours are dashed and the zero contour is omitted.

First, focusing on the polar numerical noise, several approaches are attempted and tested. In the zonal flow over a mountain test case, compared with the GAMIL-SW, the new model with u -at-pole configuration presents polar noise, which demonstrates that the nonlinear momentum advection is not the root source of the noise but may have a transmission role. The new model with v -at-pole exhibits no polar noise at all, which implies that the calculation of PV or relative vorticity near the pole is crucial. In addition, the noise present on the new model with u -at-pole is prohibited completely if the ring of relative vorticity closest to the pole is calculated using Stokes' theorem. Furthermore, potential enstrophy dissipation is not able to suppress the noise. These analysis results are confirmed by another cross-polar flow test case. Thus, it is reasonable to argue that the polar noise is related to the form of the equation and numerical treatment of the pole on the lat-lon grid, and probably belongs to an unphysical mode that is not easy to overcome by potential enstrophy dissipation. Selecting the vector-invariant momentum equation and v -at-pole configuration on the lat-lon grid is a better choice, although at the cost of an explicit time step for the finite-difference scheme.

Second, the new model performs as well or better than GAMIL-SW on another three test cases. Rossby-Haurwitz waves can be simulated steadily for three circulations and the difference from the spectral model is indistinguishable, which is as well as GAMIL-SW and much better than the model with the same scheme applied on the quasi-uniform meshes. As expected, the same as GAMIL-SW, the new model converges to second-order accuracy in the geostrophic flow test case, and the error of the new model is less than that of GAMIL-SW in terms of absolute accuracy at the same resolution. The simulation results for a barotropically unstable zonal jet are nearly identical to the results of GAMIL-SW and the spectral model.

Finally, our future goal is to develop a high-resolution atmospheric non-hydrostatic model. The development and assessment of the shallow-water model in this study has helped us to identify an appropriate horizontal momentum equation. Moreover, from the view point of computational efficiency associated with the convergence of meridians toward the pole on the lat-lon grid, a practical method for this issue will appear in a forthcoming paper.

Appendix A The Expression of Kinetic Energy in Discretization

Omitting the nonlinear Coriolis force and potential gradient terms, the thickness and momentum equation in semi-discrete form can be written as

$$\frac{\partial h_i}{\partial t} + \frac{1}{A_i} \sum_{e \in EC(i)} n_{e,i} F_e l_e = 0, \quad (A1)$$

$$\frac{\partial u_e}{\partial t} + \frac{1}{d_e} \sum_{i \in CE(e)} -n_{e,i} K_i = 0 \quad (A2)$$

where u_e denotes the normal velocity at the edge point; thus, $F_e = \hat{h}_e u_e$ denotes the normal mass flux. $e \in EC(i)$ denotes the edges that define the boundary of the primal cell, and $i \in CE(e)$ denotes two primal mesh cells that share edge e . $n_{e,i}$ is an indicator following Ringler et al. (2010), which denotes the outward or inward normal flux F_e to the cell. K_i is the kinetic energy at the primal cell to be specified. The time derivate of discrete kinetic energy in one primal cell can be obtained by multiplying equation (A2) with $A_e F_e$

$$A_e \frac{\partial}{\partial t} \left[\frac{\hat{h}_e u_e^2}{2} \right] - \frac{A_e u_e^2}{2} \frac{\partial \hat{h}_e}{\partial t} + \frac{A_e F_e}{d_e} \sum_{i \in CE(e)} -n_{e,i} K_i = 0 \quad (A3)$$

Substituting the interpolation operator of $\hat{h}_e = \sum_{i \in CE(e)} \frac{A_{ie}}{A_e} h_i$ into the second term of the above equation obtains:

$$A_e \frac{\partial}{\partial t} \left[\frac{\hat{h}_e u_e^2}{2} \right] - \frac{A_e u_e^2}{2} \frac{\partial}{\partial t} \left(\sum_{i \in CE(e)} \frac{A_{ie}}{A_e} h_i \right) + \frac{A_e F_e}{d_e} \sum_{i \in CE(e)} -n_{e,i} K_i = 0 \quad (A4)$$

Summing the equation over all edges obtains:

$$\sum_e A_e \frac{\partial}{\partial t} \left[\frac{\hat{h}_e u_e^2}{2} \right] - \sum_e \frac{A_e u_e^2}{2} \frac{\partial}{\partial t} \left(\sum_{i \in CE(e)} \frac{A_{ie}}{A_e} h_i \right) + \sum_e \frac{A_e F_e}{d_e} \sum_{i \in CE(e)} -n_{e,i} K_i = 0 \quad (A5)$$

Using (A.4) in Ringler et al. (2010) and $A_e = l_e d_e / 2$ defined in Weller et al. (2012), the sum of the third term is switched from over e to over i

$$\sum_e A_e \frac{\partial}{\partial t} \left[\frac{\hat{h}_e u_e^2}{2} \right] - \sum_e \frac{A_e u_e^2}{2} \frac{\partial}{\partial t} \left(\sum_{i \in CE(e)} \frac{A_{ie}}{A_e} h_i \right) - \frac{1}{2} \sum_i K_i A_i \sum_{e \in EC(i)} n_{e,i} F_e l_e = 0 \quad (A6)$$

Substituting equation (A1) into the third term obtains:

$$\sum_e A_e \frac{\partial}{\partial t} \left[\frac{\hat{h}_e u_e^2}{2} \right] - \sum_e \frac{A_e u_e^2}{2} \frac{\partial}{\partial t} \left(\sum_{i \in CE(e)} \frac{A_{ie}}{A_e} h_i \right) + \frac{1}{2} \sum_i K_i A_i \frac{\partial h_i}{\partial t} = 0 \quad (A7)$$

Then the second term is rearranged to give:

$$\sum_e A_e \frac{\partial}{\partial t} \left[\frac{\hat{h}_e u_e^2}{2} \right] - \sum_e \sum_{i \in CE(e)} \frac{A_{ie} u_e^2}{2} \frac{\partial h_i}{\partial t} + \frac{1}{2} \sum_i K_i A_i \frac{\partial h_i}{\partial t} = 0 \quad (A8)$$

Switching the summation sequence of the second term gives:

$$\sum_e A_e \frac{\partial}{\partial t} \left[\frac{\hat{h}_e u_e^2}{2} \right] - \sum_i \sum_{e \in EC(i)} \frac{A_{ie} u_e^2}{2} \frac{\partial h_i}{\partial t} + \frac{1}{2} \sum_i K_i A_i \frac{\partial h_i}{\partial t} = 0 \quad (A9)$$

To ensure that the second and third terms can be canceled, the discrete kinetic energy is derived as:

$$K_i = \frac{1}{A_i} \sum_{e \in EC(i)} A_{ie} u_e^2 \quad (\text{A10})$$

where A_i denotes the area of primal cell and A_{ie} is the area weight of normal velocity (u_e) within one primal cell.

Acknowledgments

The new shallow-water model is hosted on the GitHub: <https://github.com/LASG-GAMIL/GMCORE> (DOI:10.5281/zenodo.3600913).

References

- Arakawa, A., & Hsu, Y.-J. G. (1990). Energy Conserving and Potential-Enstrophy Dissipating Schemes for the Shallow Water Equations. *Monthly Weather Review*, 118, 1960–1969. Retrieved from [https://doi.org/10.1175/1520-0493\(1990\)118<1960:ECAPED>2.0.CO;2](https://doi.org/10.1175/1520-0493(1990)118<1960:ECAPED>2.0.CO;2)
- Arakawa, A., & Lamb, V. R. (1977). *Computational Design of the Basic Dynamical Processes of the UCLA General Circulation Model* (Vol. 17). Elsevier.
- Arakawa, A., & Lamb, V. R. (1981). A Potential Enstrophy and Energy Conserving Scheme for the Shallow Water Equations. *Monthly Weather Review*, 109, 18–36. Retrieved from [https://doi.org/10.1175/1520-0493\(1981\)109<0018:APEAEC>2.0.CO;2](https://doi.org/10.1175/1520-0493(1981)109<0018:APEAEC>2.0.CO;2)
- Bates, J. R., & Li, Y. (1997). Simulation of Stratospheric Vortex Erosion Using Three Different Global Shallow Water Numerical Models. *Atmosphere-Ocean*, 35(sup1), 55–74. Retrieved from <https://doi.org/10.1080/07055900.1997.9687342>
- Bonaventura, L., & Ringler, T. (2005). Analysis of Discrete Shallow-Water Models on Geodesic Delaunay Grids with C-Type Staggering. *Monthly Weather Review*, 133(8), 2351–2373. Retrieved from <https://doi.org/10.1175/MWR2986.1>
- Burridge, D. M., & Haseler, J. (1977). A model for medium range weather forecasts - adiabatic formulation [Technical Report]. (4), 46. Retrieved from <https://www.ecmwf.int/node/8495>
- Chen, C., & Xiao, F. (2008). Shallow water model on cubed-sphere by multi-moment finite volume method. *Journal of Computational Physics*, 227(10), 5019 - 5044. Retrieved from <https://doi.org/10.1016/j.jcp.2008.01.033>
- Chen, Q., Gunzburger, M., & Ringler, T. (2011). A Scale-Invariant Formulation of the Anticipated Potential Vorticity Method. *Monthly Weather Review*, 139, 2614–2629. Retrieved from <https://doi.org/10.1175/MWR-D-10-05004.1>
- Ferguson, J. O., Jablonowski, C., & Johansen, H. (2019). Assessing adaptive mesh refinement (amr) in a forced shallow-water model with moisture. *Monthly Weather Review*, 147(10), 3673–3692. Retrieved from <https://doi.org/10.1175/MWR-D-18-0392.1>
- Galewsk, J., Scott, R. K., & Polvani, L. M. (2004). An initial-value problem for testing numerical models of the global shallow-water equations. *Tellus A*, 56, 429–440. Retrieved from <https://doi.org/10.3402/tellusa.v56i5.14436>
- Gassmann, A., & Herzog, H.-J. (2008). Towards a consistent numerical compressible non-hydrostatic model using generalized Hamiltonian tools. *Quarterly Journal of the Royal Meteorological Society*, 134(635), 1597–1613. Retrieved from <https://doi.org/10.1002/qj.297>
- Giraldo, F., Hesthaven, J., & Warburton, T. (2002). Nodal high-order discontinuous galerkin methods for the spherical shallow water equations. *Journal of Compu-*

- tational Physics, 181, 499 - 525. Retrieved from <https://doi.org/10.1006/jcph.2002.7139>
- Hack, J., & R.Jakob. (1992). Description of a global shallow water model based on the spectral transform method. *NCAR Tech, Note TN-343+STR*, 39.
- Ii, S., & Xiao, F. (2010). A global shallow water model using high order multi-moment constrained finite volume method and icosahedral grid. *Journal of Computational Physics*, 229(5), 1774 - 1796. Retrieved from <https://doi.org/10.1016/j.jcp.2009.11.008>
- Jablonowski, C., Oehmke, R., & Stout, Q. (2009). *Block-structured adaptive meshes and reduced grids for atmospheric general circulation models* (Vol. 367). Retrieved from <https://doi.org/10.1098/rsta.2009.0150>
- Jakob, R., Hack, J. J., & Williamson, D. L. (1993). *Solutions to the shallow water test set using the spectral transform method* (Tech. Rep. No. May). Climate and Global Dynamics Division, National Center for Atmospheric Research, Boulder, CO. doi: 10.5065/D6DZ069T
- Jakob-Chien, R., Hack, J. J., & Williamson, D. L. (1995). Spectral Transform Solutions to the Shallow Water Test Set. *Journal of Computational Physics*, 119(1), 164-187. Retrieved from <https://doi.org/10.1006/jcph.1995.1125>
- Kühnlein, C., Deconinck, W., Klein, R., Malardel, S., Piotrowski, Z. P., Smolarkiewicz, P. K., ... Wedi, N. P. (2019). FVM 1.0: a nonhydrostatic finite-volume dynamical core for the IFS. *Geoscientific Model Development*, 12, 651-676. Retrieved from <https://doi.org/10.5194/gmd-12-651-2019>
- Lauritzen, P. H., Mirin, A. A., Truesdale, J., Raeder, K., Anderson, J. L., Bacmeister, J., & Neale, R. B. (2011). Implementation of new diffusion/filtering operators in the CAM-FV dynamical core. *The International Journal of High Performance Computing Applications*, 26, 63-73. Retrieved from <https://doi.org/10.1177/1094342011410088>
- Li, L., Lin, P., Yu, Y., Wang, B., Zhou, T., Liu, L., ... Qiao, F. (2013). The flexible global ocean-atmosphere-land system model, Grid-point Version 2: FGOALS-g2. *Advances in Atmospheric Sciences*, 30(3), 543-560. Retrieved from <https://doi.org/10.1007/s00376-012-2140-6>
- Li, X., Chen, D., Peng, X., Takahashi, K., & Xiao, F. (2008). A Multimoment Finite-Volume Shallow-Water Model on the YinYang Overset Spherical Grid. *Monthly Weather Review*, 136(8), 3066-3086. Retrieved from <https://doi.org/10.1175/2007MWR2206.1>
- Lin, S.-J. (2004). A vertically lagrangian finite-volume dynamical core for global models. *Monthly Weather Review*, 132(10), 2293-2307. Retrieved from [https://doi.org/10.1175/1520-0493\(2004\)132<2293:AVLFDC>2.0.CO;2](https://doi.org/10.1175/1520-0493(2004)132<2293:AVLFDC>2.0.CO;2)
- Lin, S.-J., & Rood, R. B. (1997). An explicit flux-form semi-lagrangian shallow-water model on the sphere. *Quarterly Journal of the Royal Meteorological Society*, 123, 2477-2498. Retrieved from <https://doi.org/10.1002/qj.49712354416>
- McDonald, A., & Bates, J. R. (1989). Semi-lagrangian integration of a gridpoint shallow water model on the sphere. *Monthly Weather Review*, 117, 130-137. Retrieved from [https://doi.org/10.1175/1520-0493\(1989\)117<0130:SLIOAG>2.0.CO;2](https://doi.org/10.1175/1520-0493(1989)117<0130:SLIOAG>2.0.CO;2)
- Nair, R. D., Thomas, S. J., & Loft, R. D. (2005). A discontinuous galerkin global shallow water model. *Monthly Weather Review*, 133, 876-888. Retrieved from <https://doi.org/10.1175/MWR2903.1>
- Peixoto, P. S., Thuburn, J., & Bell, M. J. (2018). Numerical instabilities of spherical shallow-water models considering small equivalent depths. *Quarterly Journal of the Royal Meteorological Society*, 144(710), 156-171. Retrieved from <https://doi.org/10.1002/qj.3191>
- Ringler, T. D., Jacobsen, D., Gunzburger, M., Ju, L., Duda, M., & Skamarock, W.

- (2011). Exploring a Multiresolution Modeling Approach within the Shallow-Water Equations. *Monthly Weather Review*, 139(11), 3348–3368. Retrieved from <https://doi.org/10.1175/MWR-D-10-05049.1>
- Ringler, T. D., & Randall, D. A. (2002). A Potential Enstrophy and Energy Conserving Numerical Scheme for Solution of the Shallow-Water Equations on a Geodesic Grid. *Monthly Weather Review*, 130(5), 1397–1410. Retrieved from [https://doi.org/10.1175/1520-0493\(2002\)130<1397:APEAEC>2.0.CO;2](https://doi.org/10.1175/1520-0493(2002)130<1397:APEAEC>2.0.CO;2)
- Ringler, T. D., Thuburn, J., Klemp, J. B., & Skamarock, W. C. (2010). A unified approach to energy conservation and potential vorticity dynamics for arbitrarily-structured C-grids. *Journal of Computational Physics*, 229, 3065–3090. Retrieved from <https://doi.org/10.1016/j.jcp.2009.12.007>
- Sadourny, R. (1975). The dynamics of finite-difference models of the shallow-water equations. *Journal of the Atmospheric Sciences*, 32, 680–689. Retrieved from [https://doi.org/10.1175/1520-0469\(1975\)032<0680:TDOFDM>2.0.CO;2](https://doi.org/10.1175/1520-0469(1975)032<0680:TDOFDM>2.0.CO;2)
- Sadourny, R., & Basdevant, C. (1985). Parameterization of Subgrid Scale Barotropic and Baroclinic Eddies in Quasi-geostrophic Models: Anticipated Potential Vorticity Method. *Journal of the Atmospheric Sciences*, 42, 1353–1363. Retrieved from [https://doi.org/10.1175/1520-0469\(1985\)042<1353:POSSBA>2.0.CO;2](https://doi.org/10.1175/1520-0469(1985)042<1353:POSSBA>2.0.CO;2)
- Satoh, M., Tomita, H., Yashiro, H., Miura, H., Kodama, C., Seiki, T., . . . Kubokawa, H. (2014). The Non-hydrostatic Icosahedral Atmospheric Model: description and development. *Progress in Earth and Planetary Science*, 1, 18. Retrieved from <https://doi.org/10.1186/s40645-014-0018-1> doi: 10.1186/s40645-014-0018-1
- Shamir, O., & Paldor, N. (2016). A quantitative test case for global-scale dynamical cores based on analytic wave solutions of the shallow-water equations. *Quarterly Journal of the Royal Meteorological Society*, 142(700), 2705–2714. Retrieved from <https://doi.org/10.1002/qj.2861>
- Skamarock, W. C. (2008). A linear analysis of the near ccsm finite-volume dynamical core. *Monthly Weather Review*, 136(6), 2112–2119. Retrieved from <https://doi.org/10.1175/2007MWR2217.1>
- Skamarock, W. C., Klemp, J. B., Duda, M. G., Fowler, L. D., Park, S.-H., & Ringler, T. D. (2012). A Multiscale Nonhydrostatic Atmospheric Model Using Centroidal Voronoi Tessellations and C-Grid Staggering. *Monthly Weather Review*, 140, 3090–3105. Retrieved from <https://doi.org/10.1175/MWR-D-11-00215.1>
- Staniforth, A., & Thuburn, J. (2012). Horizontal grids for global weather and climate prediction models: A review. *Quarterly Journal of the Royal Meteorological Society*, 138, 1–26. Retrieved from <https://doi.org/10.1002/qj.958>
- Takano, K., & Wurtele, M. G. (1982). *A fourth order energy and potential enstrophy conserving difference scheme* (Tech. Rep.).
- Thuburn, J. (2008). Some conservation issues for the dynamical cores of NWP and climate models. *Journal of Computational Physics*, 227, 3715–3730. Retrieved from <https://doi.org/10.1016/j.jcp.2006.08.016>
- Thuburn, J. (2013). Computational Modes in Weather and Climate Modes. *ECMWF Seminar on Numerical Methods for Atmosphere and Ocean Modelling, 2-5 September 2013*, 213–226.
- Thuburn, J., & Cotter, C. (2012). A Framework for Mimetic Discretization of the Rotating Shallow-Water Equations on Arbitrary Polygonal Grids. *SIAM Journal on Scientific Computing*, 34, B203–B225. Retrieved from <https://doi.org/10.1137/110850293>
- Thuburn, J., Cotter, C. J., & Dubos, T. (2014). A mimetic, semi-implicit, forward-in-time, finite volume shallow water model: comparison of hexagonalicosahedral and cubed-sphere grids. *Geoscientific Model Development*, 7(3), 909–929. Retrieved from <https://doi.org/10.5194/gmd-7-909-2014>

- Thuburn, J., & Li, Y. (2000). Numerical simulations of Rossby-Haurwitz waves. *Tellus A*, 52, 181–189. Retrieved from <https://doi.org/10.3402/tellusa.v52i2.12258>
- Thuburn, J., Ringler, T. D., Skamarock, W. C., & Klemp, J. B. (2009). Numerical representation of geostrophic modes on arbitrarily structured C-grids. *Journal of Computational Physics*, 228, 8321–8335. Retrieved from <https://doi.org/10.1016/j.jcp.2009.08.006>
- Thuburn, J., & Staniforth, A. (2004). Conservation and Linear Rossby-Mode Dispersion on the Spherical C Grid. *Monthly Weather Review*, 132, 641–653. Retrieved from [https://doi.org/10.1175/1520-0493\(2004\)132<0641:CALRDO>2.0.CO;2](https://doi.org/10.1175/1520-0493(2004)132<0641:CALRDO>2.0.CO;2)
- Tomita, H., Tsugawa, M., Satoh, M., & Goto, K. (2001). Shallow Water Model on a Modified Icosahedral Geodesic Grid by Using Spring Dynamics. *Journal of Computational Physics*, 174(2), 579–613. Retrieved from <https://doi.org/10.1006/jcph.2001.6897>
- Ullrich, P. A., Jablonowski, C., Kent, J., Lauritzen, P. H., Nair, R., Reed, K. A., ... Viner, K. (2017). DCMIP2016: A review of non-hydrostatic dynamical core design and intercomparison of participating models. *Geoscientific Model Development*, 10(12), 4477–4509. Retrieved from <http://dx.doi.org/10.5194/gmd-10-4477-2017>
- Wang, B., & Ji, Z. (2003). Construction and numerical tests of the multi-conservation difference scheme. *Chinese Science Bulletin*, 48(10), 1016–1020. Retrieved from <https://doi.org/10.1007/BF03184218>
- Wang, B., & Ji, Z. (2006). *New numerical methods and their applications in the atmospheric science*. science press. (208pp)
- Wang, B., Wan, H., Ji, Z., Zhang, X., Yu, R., Yu, Y., & Liu, H. (2004). Design of a new dynamical core for global atmospheric models based on some efficient numerical methods. *Science in China Series A*, 47, 4. Retrieved from <https://doi.org/10.1360/04za0001>
- Wang, B., Zhou, T., Yu, Y., & Wang, B. (2009). A view of earth system model development. *Acta Meteorologica Sinica*, 23(1), 1–17.
- Weller, H. (2012). Controlling the Computational Modes of the Arbitrarily Structured C Grid. *Monthly Weather Review*, 140, 3220–3234. Retrieved from <https://doi.org/10.1175/MWR-D-11-00221.1>
- Weller, H., Thuburn, J., & Cotter, C. J. (2012). Computational Modes and Grid Imprinting on Five Quasi-Uniform Spherical C Grids. *Monthly Weather Review*, 140, 2734–2755. Retrieved from <https://doi.org/10.1175/MWR-D-11-00193.1>
- Whitehead, J. P., Jablonowski, C., Rood, R. B., & Lauritzen, P. H. (2011). A Stability Analysis of Divergence Damping on a LatitudeLongitude Grid. *Monthly Weather Review*, 139, 2976–2993. Retrieved from <https://doi.org/10.1175/2011mwr3607.1>
- Williamson, D. L., Drake, ., Hack, ., Jakob, ., & Swarztrauber, . (1992). A standard test set for numerical approximations to the shallow water equations in spherical geometry. *Journal of Computational Physics*, 102, 211–224. Retrieved from [https://doi.org/10.1016/S0021-9991\(05\)80016-6](https://doi.org/10.1016/S0021-9991(05)80016-6)
- Worley, P. H., & Toonen, B. (1995). *A Users' Guide To Pstswm*.
- Yu, Y., Zhi, H., Wang, B., Wan, H., Li, C., Liu, H., ... Zhou, T. (2008). Coupled model simulations of climate changes in the 20th century and beyond. *Advances in Atmospheric Sciences*, 25(4), 641–654. Retrieved from <https://doi.org/10.1007/s00376-008-0641-0>
- Zängl, G., Reinert, D., Rípodas, P., & Baldauf, M. (2015). The ICON (ICOsa-hedral Non-hydrostatic) modelling framework of DWD and MPI-M: Description of the non-hydrostatic dynamical core. *Quarterly Journal of the Royal Meteorological Society*, 141(687), 563–579. Retrieved from

- 956 <https://doi.org/10.1002/qj.2378>
957 Zeng, Q., & Zhang, X. (1987). Finite difference scheme keeping the effective en-
958 ergy conservation of the spherical primitive equation set for the baroclinic
959 atmosphere. *Chinese Journal of Atmospheric Sciences*, 11, 113-127.
960 Zeng, Q., Zhang, X., Liang, X., & Chen, S. (1989). *Document of IAP two-level at-*
961 *mospheric general circulation model*. DOE/ER/60314-HI, U. S. Department of
962 Energy, Washington, D. C. (383pp)
963 Zhang, X. (1990). Dynamical framework of IAP nine-level atmospheric general cir-
964 culation model. *Advances in Atmospheric Sciences*, 7, 67-77. Retrieved from
965 <https://doi.org/10.1007/BF02919169>

Figure 1.

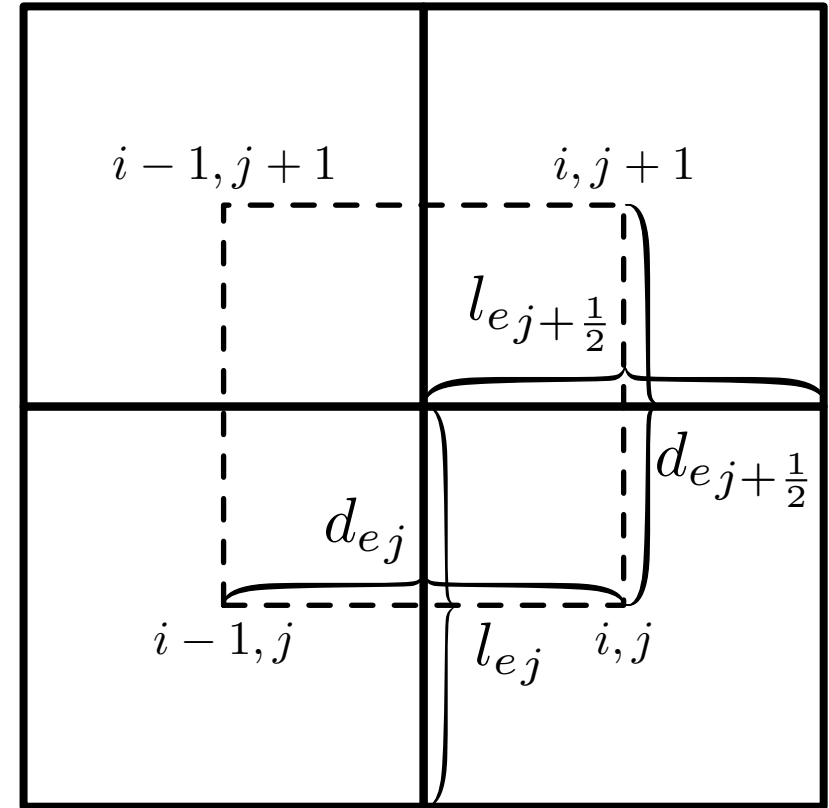
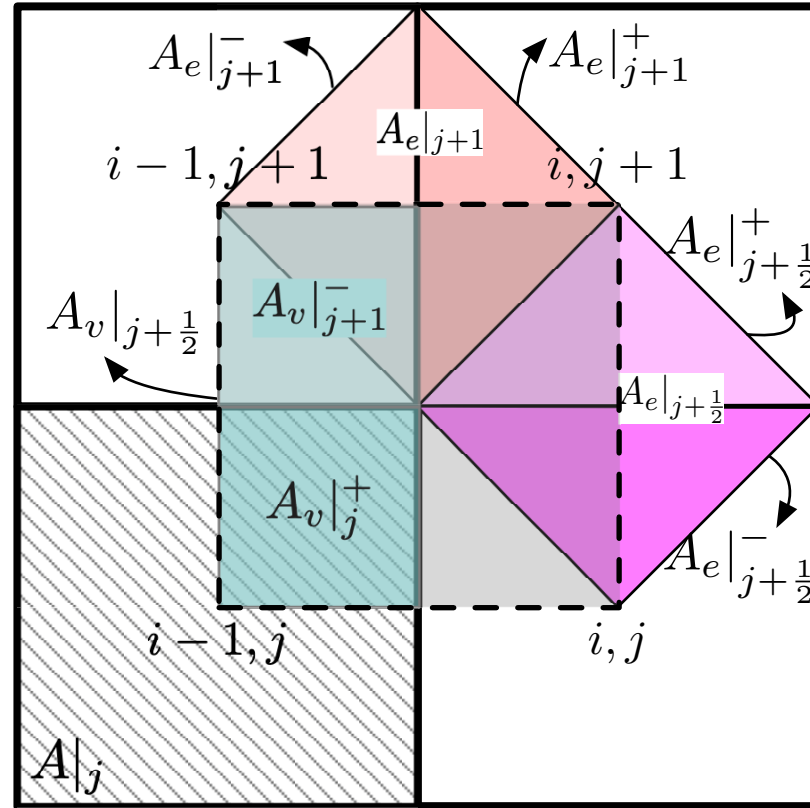
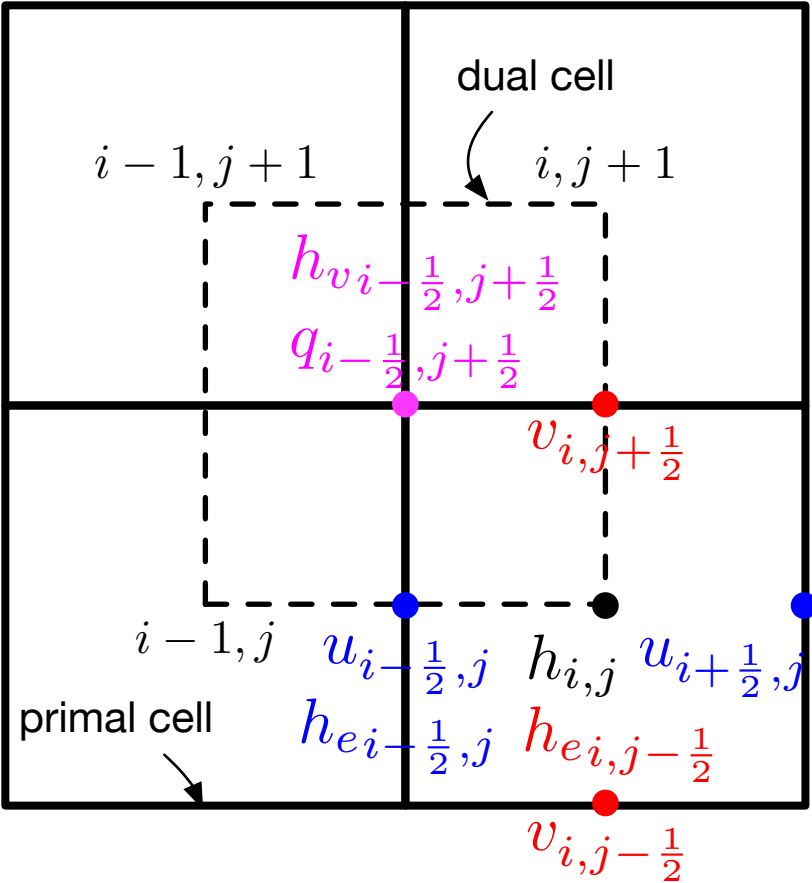


Figure 2.

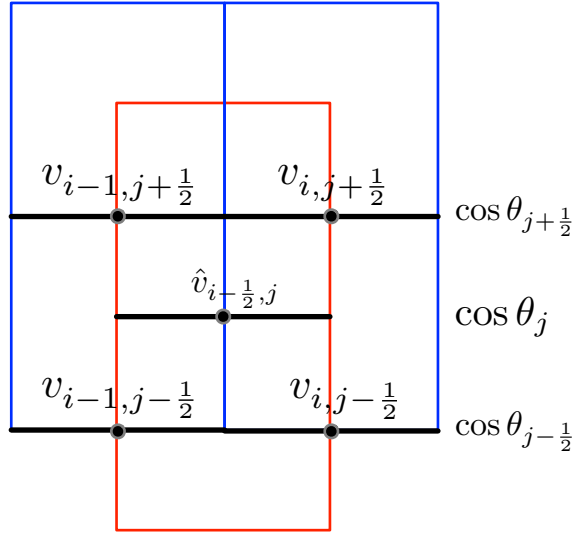
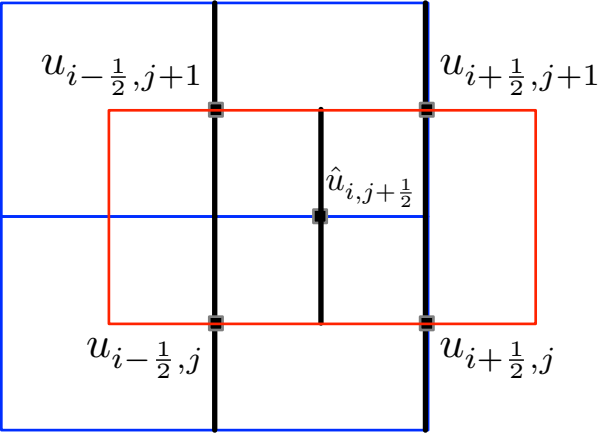


Figure 3.

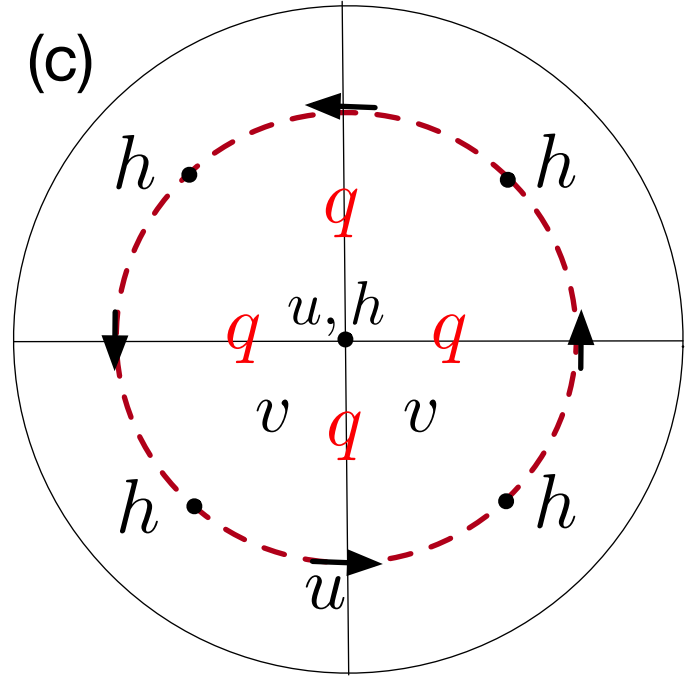
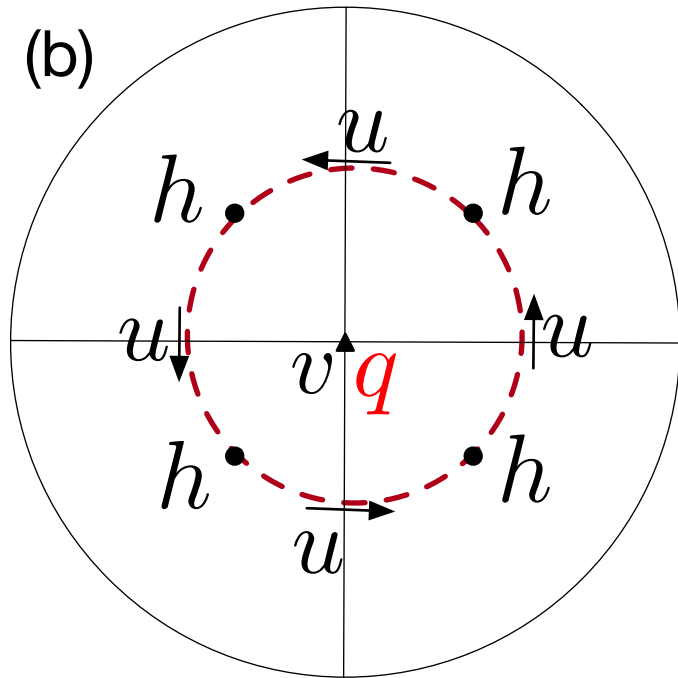
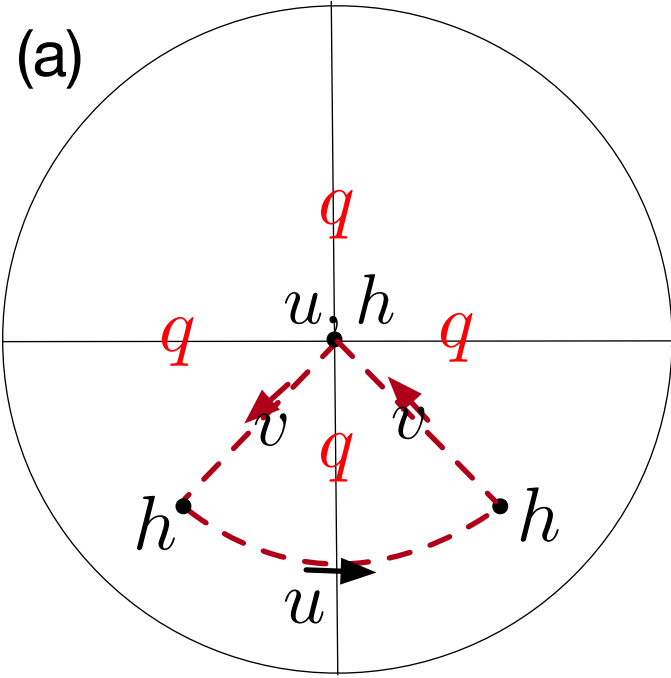


Figure 4.

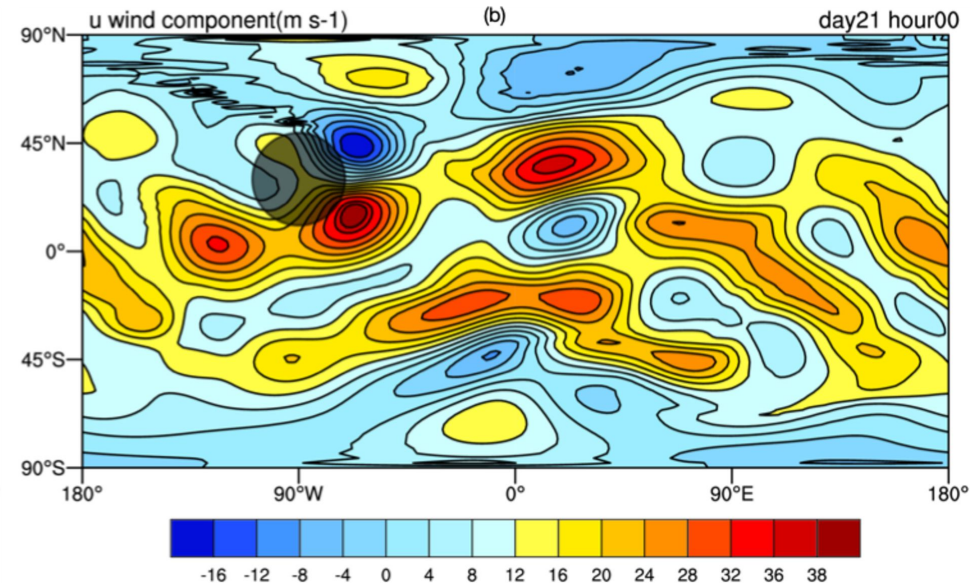
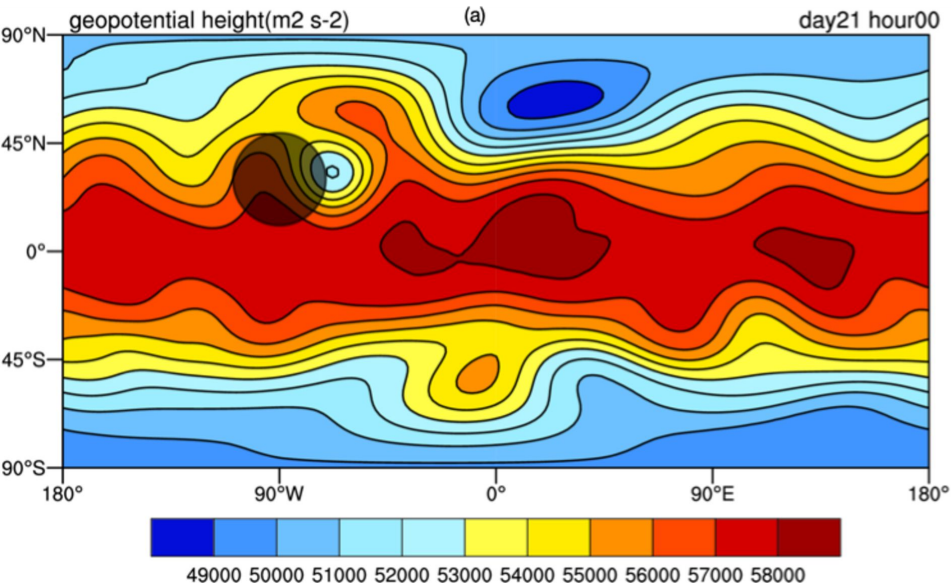


Figure 5.

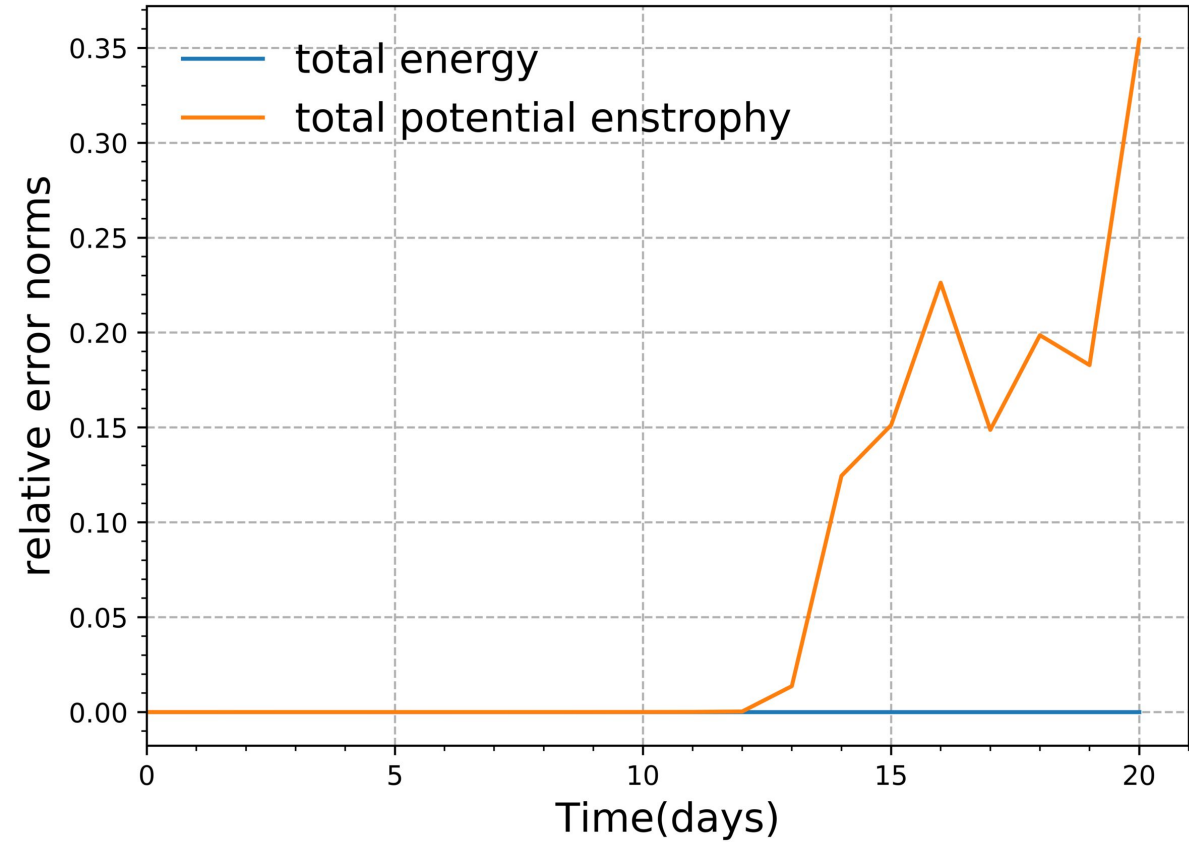


Figure 6.

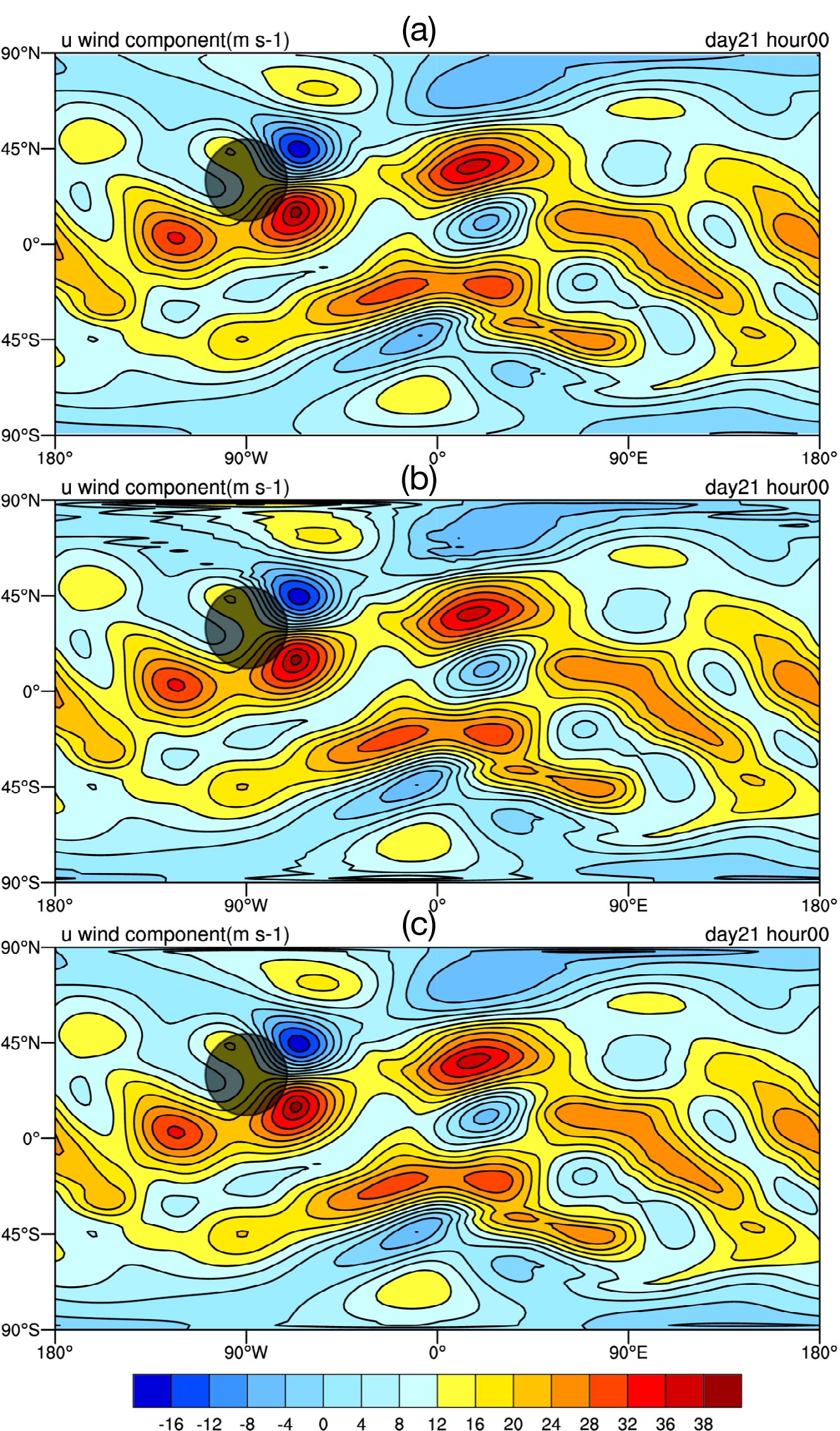


Figure 7.

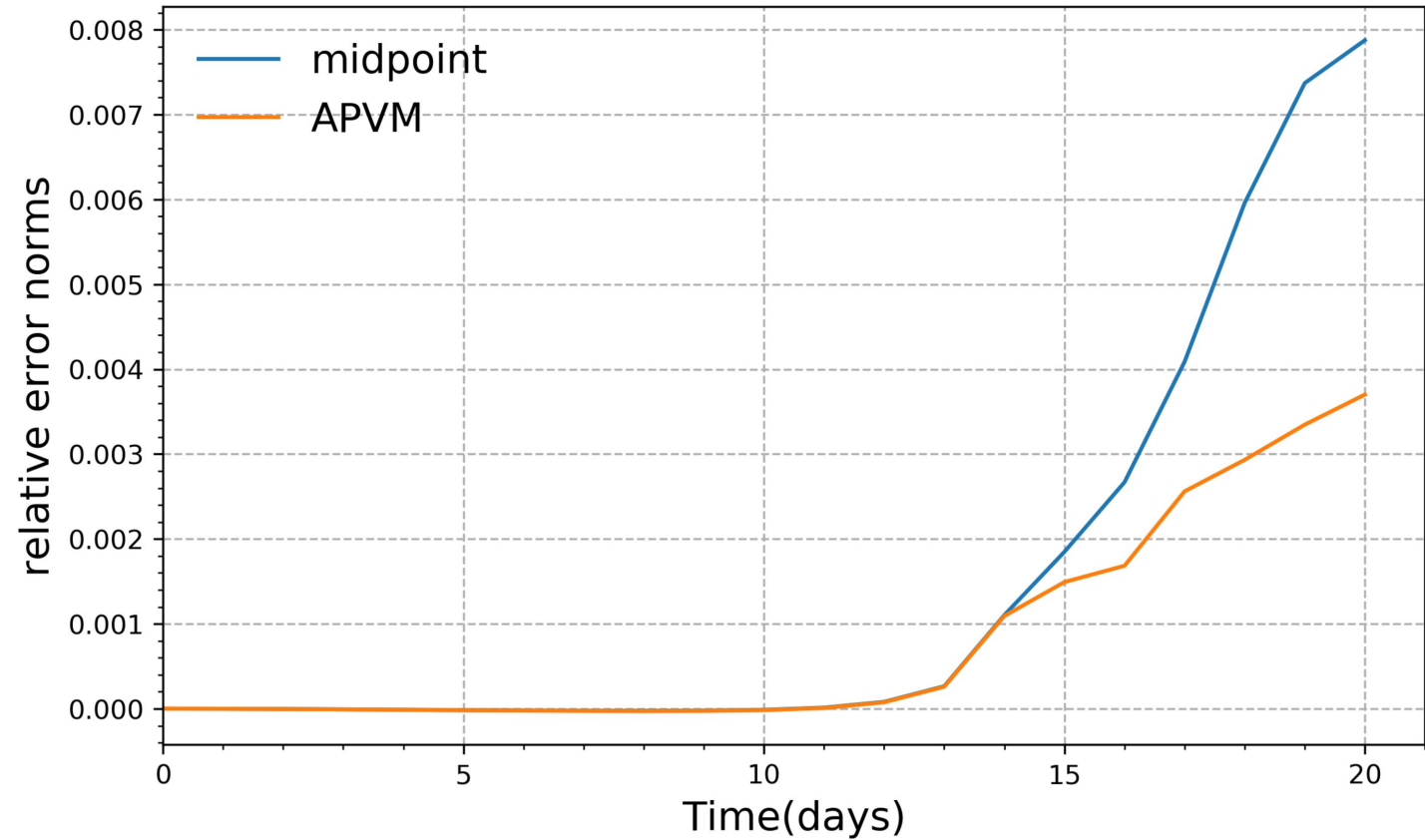


Figure 8.

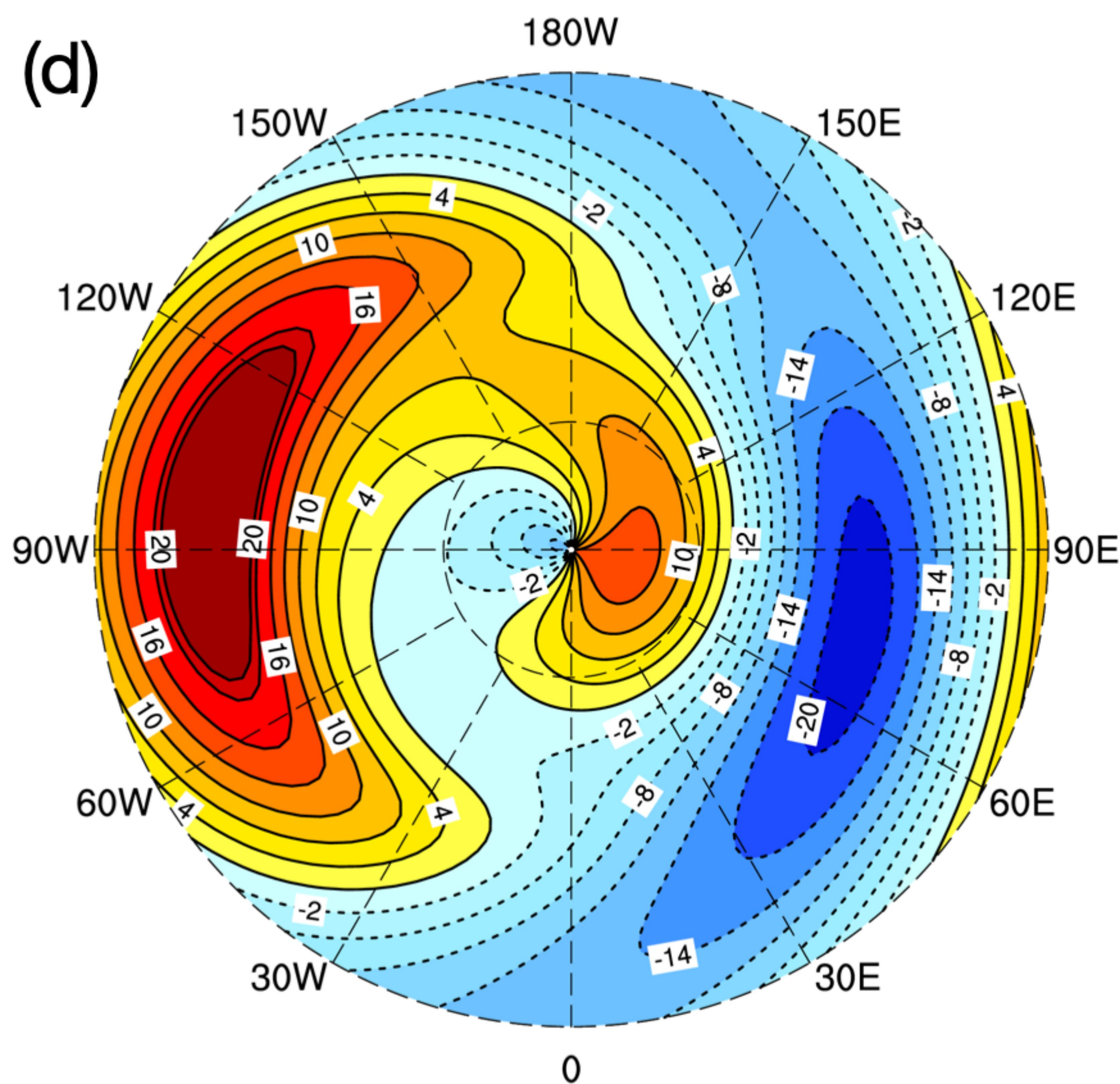
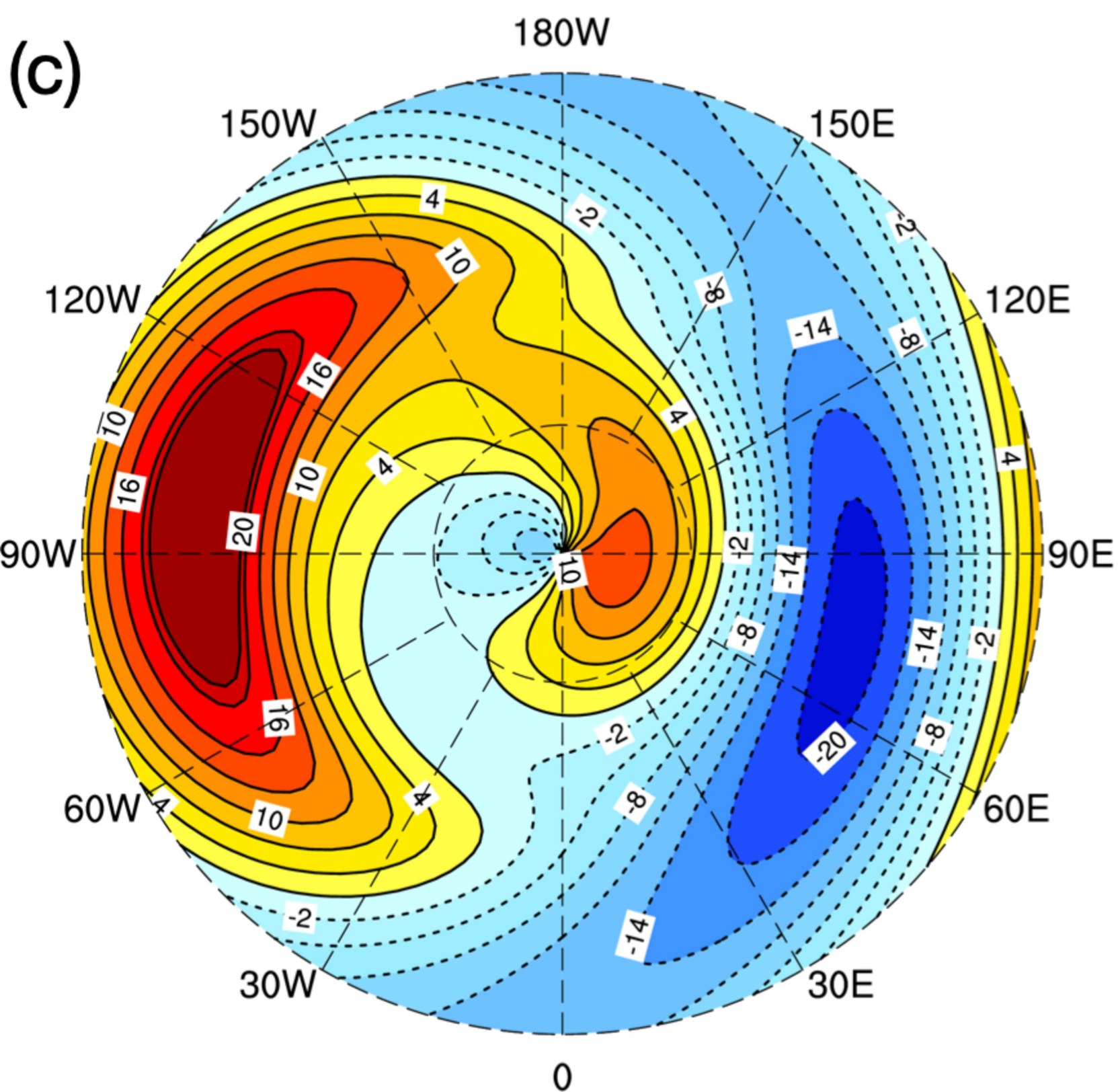
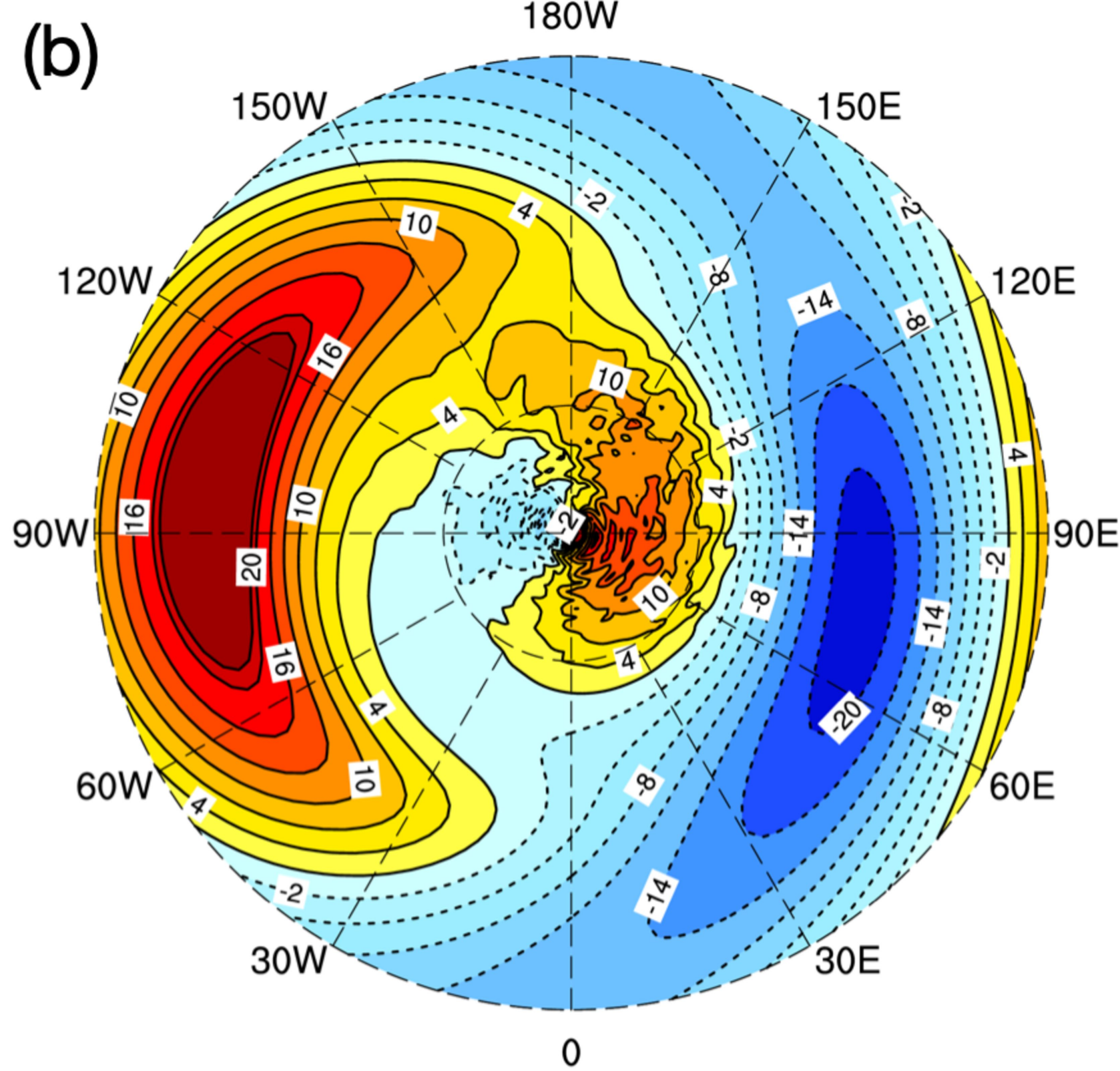
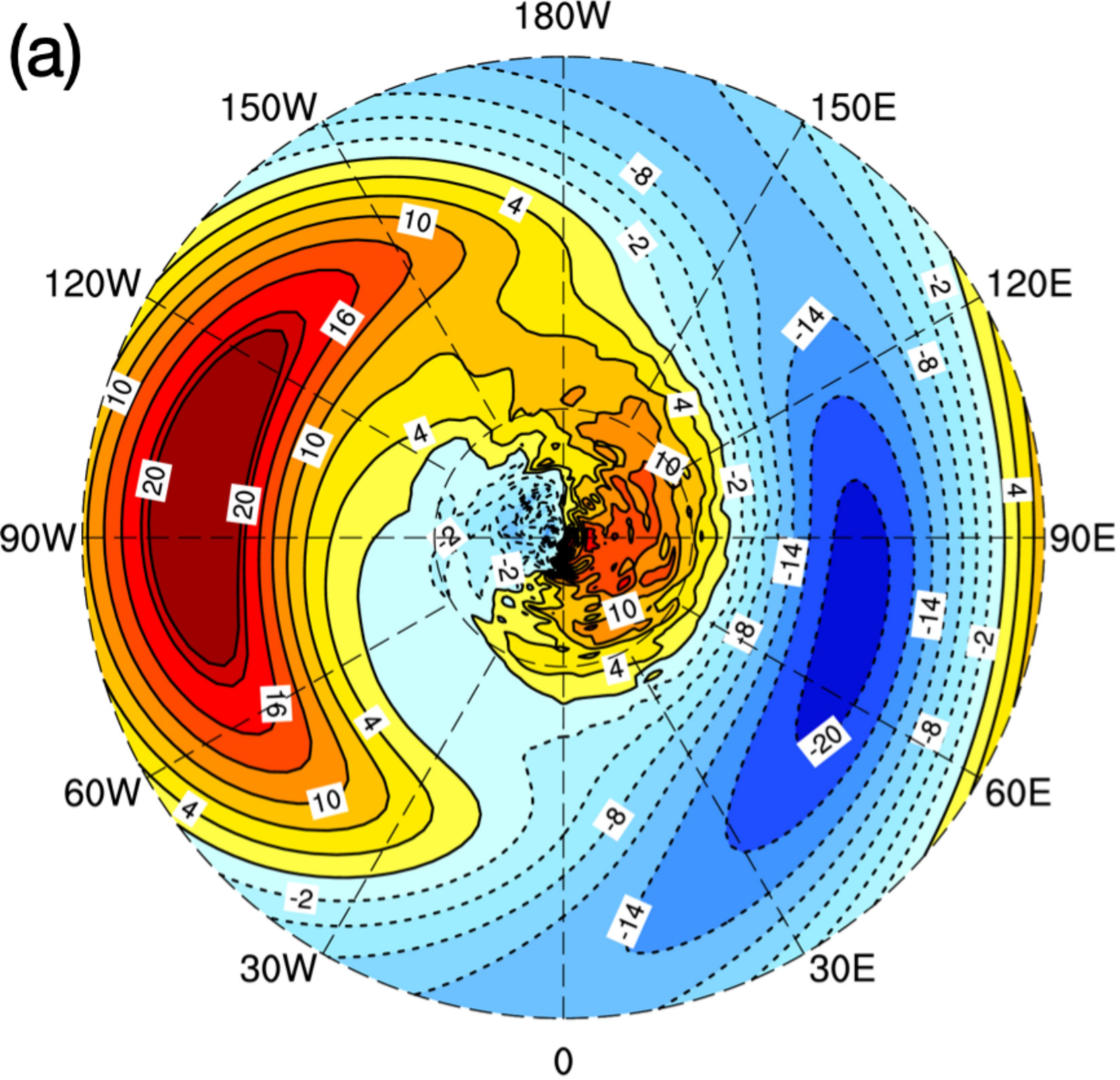


Figure 9.

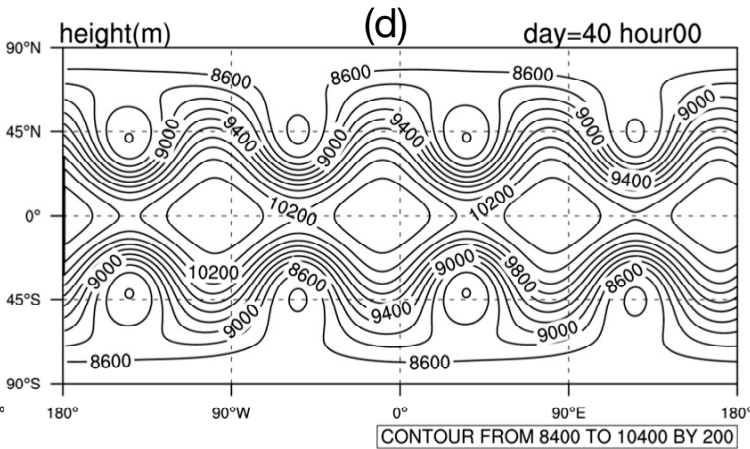
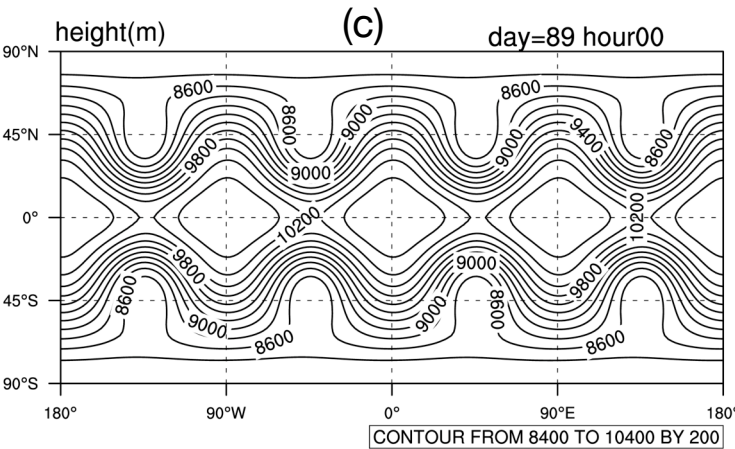
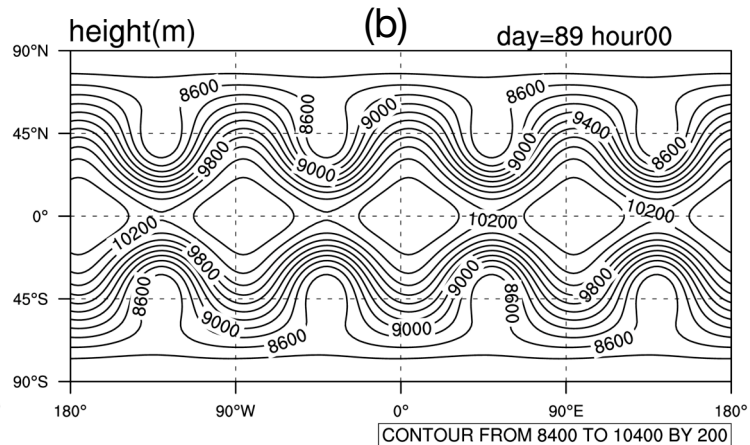
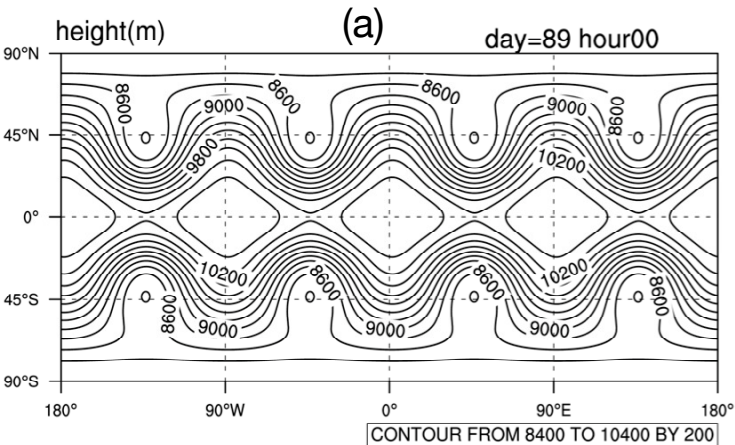


Figure 10.

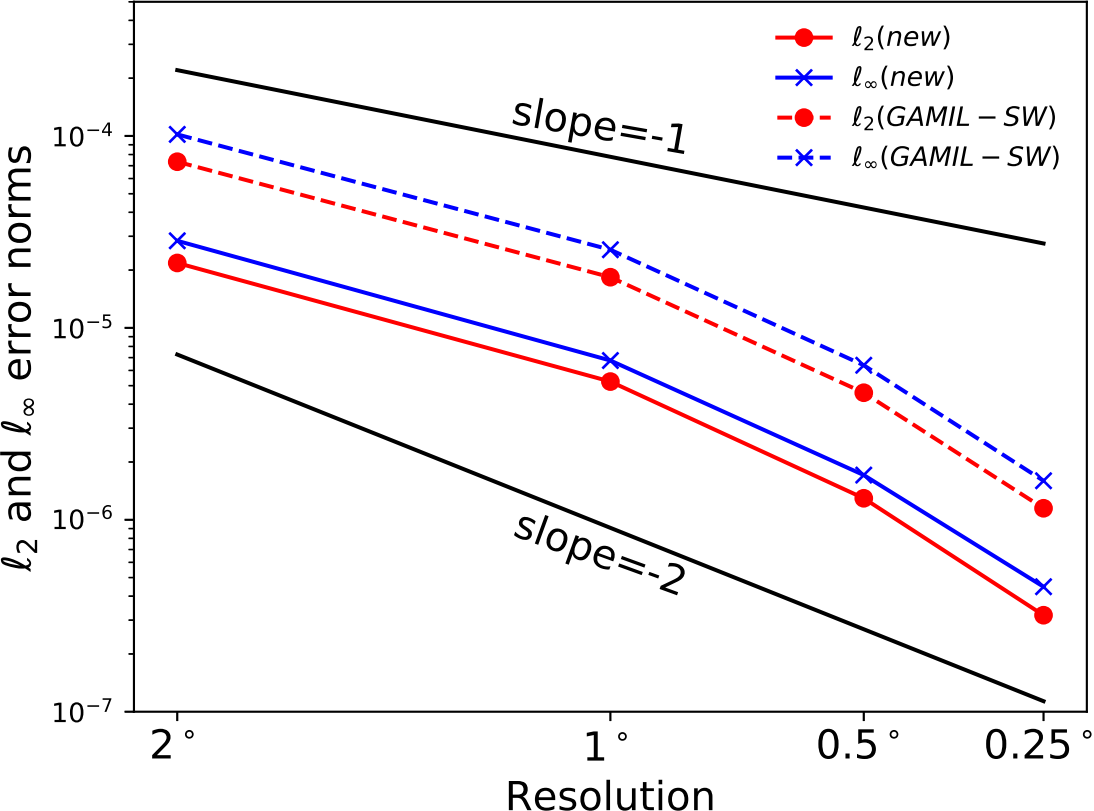
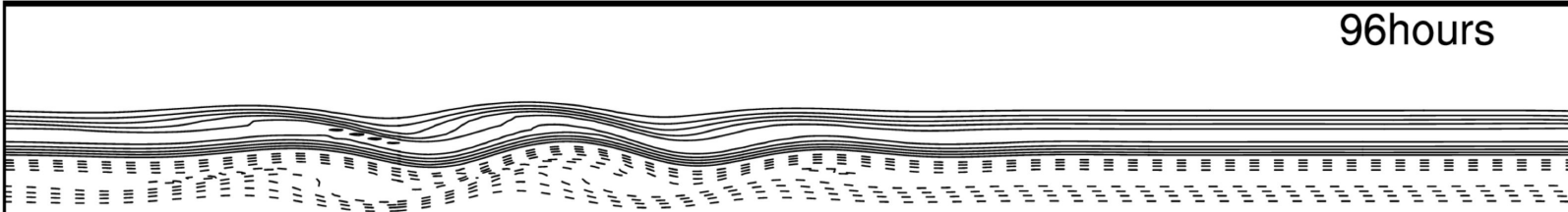


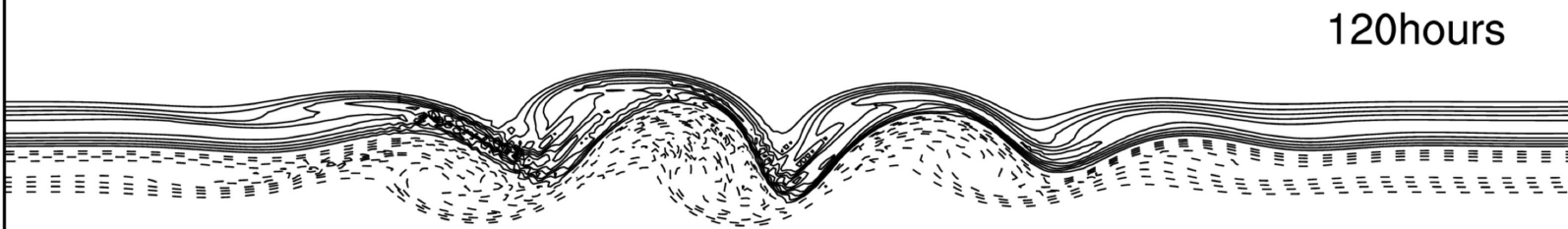
Figure 11.

(a)

96hours



120hours

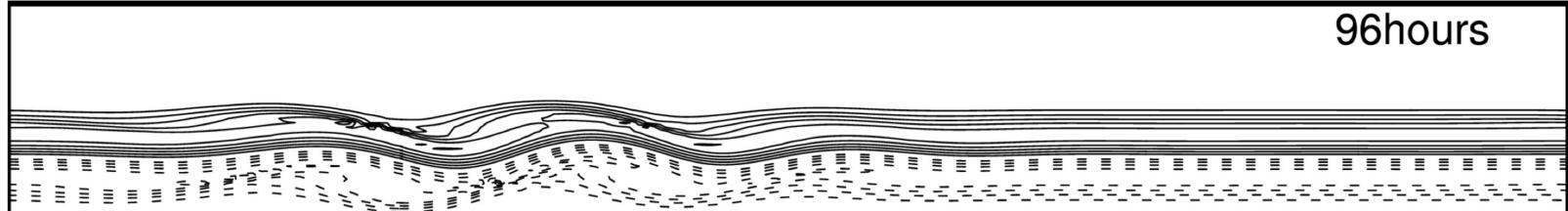


144hours

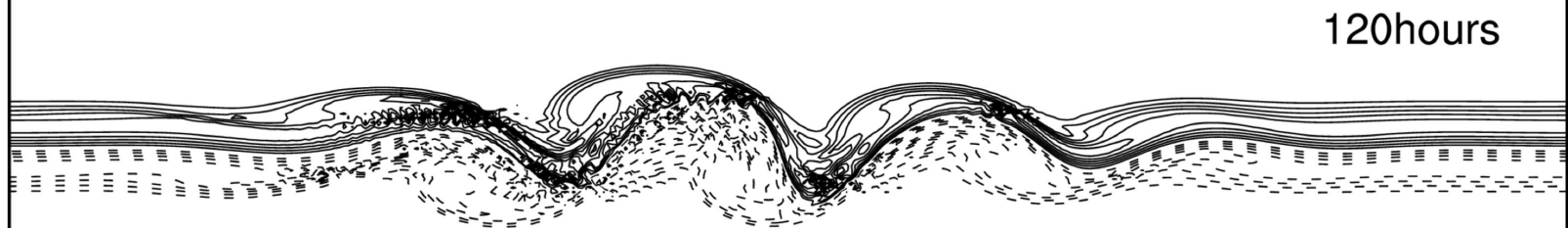


(b)

96hours



120hours



144hours

